Mesoscopic and Statistical Properties of Fluctuating Membranes

Diplomarbeit

Ronald Holzlöhner
Matr. Nr. 124930

1. Gutachter: Prof. Dr. S. Hess
2. Gutachter: Dr. rer. nat. habil. M. Schoen

Institut für Theoretische Physik
Technische Universität Berlin

6. August 1998

The most exciting phrase to hear in science, the one that heralds new discoveries, is not "Eureka!" (I found it!) but "That's funny . . . "

Isaac Asimov

Contents

Introduction

In nature, constraints in some systems often lead to an even richer, more complex behavior than it would be encountered in their absence. In physics, prominent examples are found in quantum mechanics, where localization of particles leads to quantization of their energy states, as compared to continuous spectra for vanishing potentials [Mes64]. Confinement of an electron gas to two, one, or even zero dimensions is essential for the Quantum Hall effect and the physics of quantum dots [BW95]. The existence of "forbidden" electron transitions increase the life time of excited states in gas lasers [Hak70].

Also in thermodynamics, there are numerous cases where the introduction of confinements changes the overall behavior. Spatial confinements such as limited system size and excluded volume interactions, play an important role in many physical laws [Hil64, Sch97].

In mathematics, a major part of differential geometry deals with manifolds with an intrinsic dimension smaller than that of the space they are embedded in [Spi70]. The topic of this thesis are the properties of fluctuating surfaces in three-dimensional space. Here, these surfaces may consist of molecules which are bound together to membranes. The membranes are corrugated, but the corresponding curvature radii are far beyond the molecular length scale. This research field can be regarded as part of polymer physics, however, membranes show some important differences in their behavior as compared to linear polymers, often due to geometric constraints [DE86].

The behavior of pure, "naked" membranes is interesting enough and still being investigated intensively. One way to extend this simple system is to decorate the surface by embedding inclusions, whose interaction with each other and the ambient membrane opened up a whole new area of research [SI89, GBP93].

Biological cells have walls which constitute the basic compartment in the bodies of most animals, plants, and even bacteria. These walls are called *lipid membranes* and show complex behavior that is often investigated in molecular biology. Proteins and polymers are included in these surfaces and serve e.g. as ion pumps to sustain the life functions of the cell [HLMZ77, Ack92]. Recently, synthetic lipid membranes have been used in medicine to "mask" (wrap) special types of drugs, which are more or less poisonous and have to be transported in the blood system for example directly to the locus of a tumor. Also, there are recent applications to enclose tiny gas bubbles in lipid membranes which, upon injection in a vein, enhance the contrast in ultrasonic sonographs of organs. Using gas bubbles is favorable due to the corresponding harsh density gradient on their surface which yields large contributions in (Rayleigh) scattering theory,

but would lead to embolisms if unmasked [SHLU93].

Deriving laws that govern the behavior of fluctuating membranes in a purely analytical way is very hard, although a couple of notable predictions were found that way. Theoretical treatments started out in the early seventies based on differential geometry and of course statistical mechanics [Can70, Hel73]. Methods such as renormalization group (RG) calculations and perturbation theory were employed later to find scaling laws and phase transitions [Hel85, Pel86, Dav88]. However, to test these results and give new input to theory, numerical simulation is another cornerstone of research efforts and the link to experiment.

The goal of this thesis is to compare the results of a Monte Carlo simulation of a bending stiff, fluid, closed random surface with theory. As an extension, anisotropic, rigid particles are simulated on this surface. The membrane thus serves as a laboratory for simulating statistical mechanics in a special geometry.

In chapter I, the physics of biological membranes will be discussed as a motivation and base for later models. Chapter II deals with the derivation of a bending Hamiltonian and its microscopic justification by molecular forces. In chapter III, the connection with thermodynamics is treated, both for the pure membrane and with particles embedded in it. Also, characteristic lengths are defined. Chapter IV is devoted to theoretical foundations of the Monte Carlo method, chapter V describes the program that was developed, and its results are presented in chapter VI. In chapter VII, the results are reviewed and an outlook for future research is given.

Some mathematical details are summarized in the appendix.

I. Lipid Membranes

I.1 What is a Lipid Membrane?

This chapter aims at describing physical and biological properties of lipid membranes in nature.

Biological lipid membranes constitute the basic building blocks of all cells. Also, they serve as functional elements, being both a barrier between in- and outside of a cell and carrying larger molecules such as inclusions that are permeable for specific chemicals.

A lipid molecule consists of a hydrophilic (water-loving) head group and one or two hydrophobic (water-repelling) hydrocarbon tails. This property is called *amphiphilic*; corresponding chemicals include fats, tensids, and some liquid crystals. Often *phospholipids* are encountered, since most of the biological lipids contain a phosphor atom in their head group. Typical chemical compounds include *dipalmitoyl-phosphatidyl-cholin* (DPPC) and *dimyristoyl-phosphatidyl-cholin* (DMPC, Fig. I.1), the latter having for instance two tail chains of 13 carbon atoms each (see also Fig. II.2). Also natural mixtures such as *egg yoke phosphatidyl-choline* (EYPC) appear frequently. When immersed in a polar solvent such as water, they spontaneously form aggregates (Fig. I.2) such as layers (a) or so-called micelles (b). This aggregation is driven by a corresponding lowering of potential energy, as hydrophobic parts can be "hidden" from the solvent that way and the number of hydrogen bonds in the water can be maximized. Two lipid layers usually form a *bilayer* (Fig. I.3) by joining two monolayers on the tail side. The typical thickness of a bilayer is 4-6 nanometers and thus wave microscopy is difficult even in the X-ray range. Common structures that bilayers can assume are *vesicles*, which are closed surfaces (bubbles) of a diameter from 40 nm up to a few hundred nanometers [HLMZ77]. Vesicles are the structures considered in this thesis, as they both constitute important biological systems and can be simulated easily [GK95].

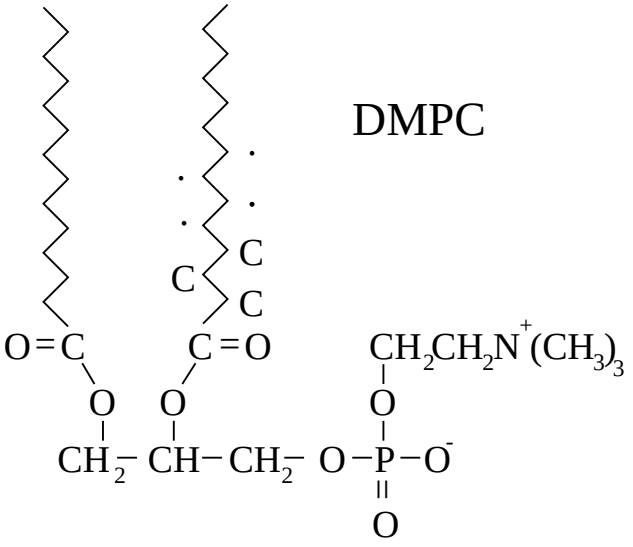

***Figure** I.1: Chemical structure of DMPC. The two tail chains contain 13 carbon atoms each.*

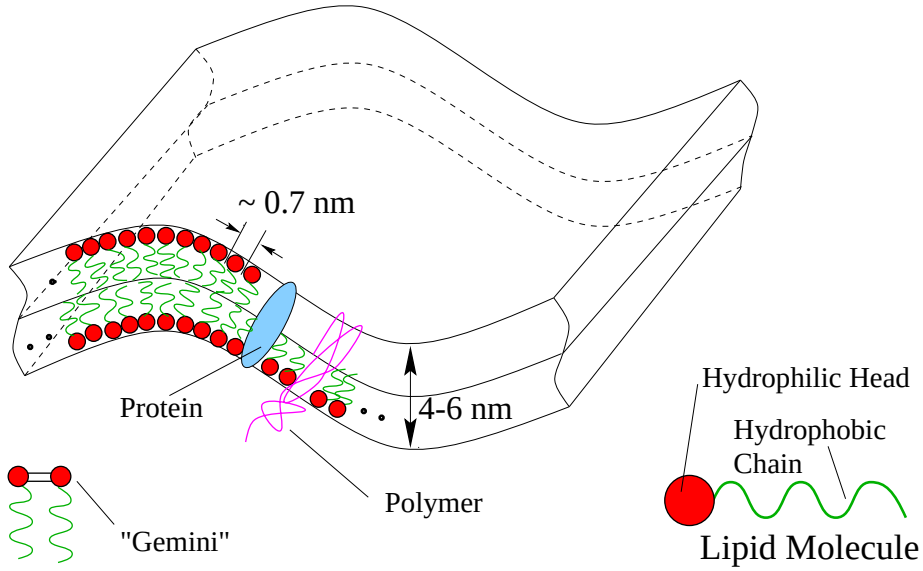

***Figure** I.3: Section of a lipid bilayer with some typical inclusions.*

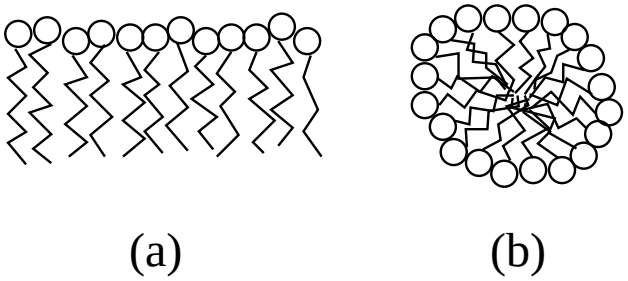

***Figure** I.2: Lipid layer (a) and micelle (b).*

First proposals of the bilayer structure were published as early as 1925 by Gorter and Grendel (see references in [HLMZ77]). They compared the amount of lipids extracted from dissolved cell walls of known surface area with a monolayer floating on a water surface and found a ratio of about two. The parallel "palisade" alignment of the tails was indicated even before by polarization-microscopy, when it was shown that nerve tissue is strongly birefringent [HLMZ77]. Freeze-fracture experiments with subsequent etching showed that lipid membranes break preferably along inner planes, which further supports bilayer theories. Modern imaging methods include cryo-transmission electron-microscopy (cryo-TEM, see Fig. I.5), scanning tunnel-, and atomic force microscopy (STM, AFM).

I.2 Phases

Perhaps the most stunning feature of lipid membranes is their fluidity: The shear modulus in the membrane plane is low, correspondingly, the lateral diffusion coefficient of lipids or embedded test particles is quite high. This makes lipid membranes appear as a viscous *2D-fluid*. Moreover, at least in some temperature range, translational symmetry is only broken in the direction normal to the plane, i.e., the bilayer shows rotational

and in-plane translational symmetry. This is the symmetry of a smectic-A liquid crystal [Mac97] and therefore this phase is also called *liquid crystal phase*. Multiple bilayers in addition often assemble in stacked-up sheets, known as the *lamellar fluid phase*.

As temperature is lowered, a first-order transition from the lamellar fluid phase (L_α) to a so-called *gel phase* (L_β) is observed (Fig. I.4). For DMPC, this occurs around $T_t \approx 45\,^\circ$C. This gel phase is characterized by freezing of the lipid tails into a six-fold symmetry, the *hexatic phase* develops.

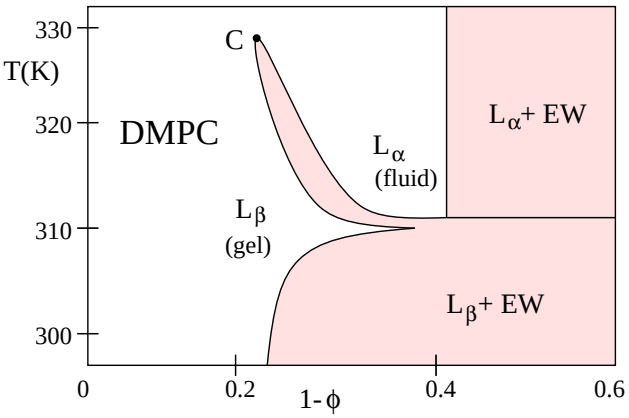

***Figure** I.4: Qualitative phase diagram for DMPC as a function of lipid volume fraction ϕ. "EW" denotes excess water, "C" is the triple point (reproduced after [GL89]).*

In addition to these two simple phases, many more sub–phases have been found, depending on the chemical and mechanical properties of the constituents. These include for instance the *"ripple"–phase* [Mac97] in which the membrane forms a superstructure in the shape of an egg-carton. This was investigated in the Studienarbeit [Hol97]. Superstructures are of special interest in the scope of this work since they introduce an intermediate, mesoscopic length scale between microscopic (lipid head size: ca. 0.7 nm) and "macroscopic" (some 100 nm) lengths. Internal degrees of freedom such as chirality or molecular tilt [LM93, ML91, GL89], as well as anisotropic inclusions [Fou96, Hol97], see Fig. I.5, were employed to explain this phase by breaking the in-plane symmetry. A global molecular tilt would correspond to a smectic-C liquid crystal. All these biological data are important to find a reasonable simplified model for the Monte Carlo simulation, as explained in chapters IV and V.

I.3 Further Mechanical Properties

Fluidity enables lipid membranes to form cusps and in extreme cases even elongated branches ("dumbbells"). Besides fluidity (at least in the fluid phase), lipid membranes have two other essential characteristics: Vanishing surface tension and finite bending stiffness [Isr92, HLMZ77, Lip98]. This is somehow opposite from soap bubbles: A soap-water solution is a (3D-)isotropic fluid, which tries to minimize its energetically unfavorable interface to the air. Thus, a global surface tension results. On the other hand, the curvature of the bubble does not directly influence its internal energy, since at least the bulk of the soap film (the shell of a typical soap bubble might have a thickness of several tens of microns) does not feel curvature due to its isotropy.

In contrast, the surface area of a lipid membrane is more or less determined by its total

number of lipids since the membrane is a monomolecular sheet (see also the next chapter). Strong stretching of the membrane just leads to tearing, whereas compression induces a corrugation, without changing the true surface area, either.

In addition, curving a lipid membrane leads to splay of the lipids, which can be seen in Figs. I.2 and I.3. This implies a deviation from the preferred intermolecular distances, which results in an intrinsic bending rigidity. In the physical literature, thin surface tension controlled systems are referred to as "films", as opposed to bending stiff "membranes". A 2D-fluid that resists curving is quite strange to everyday experience and a macroscopic mechanical model hard to conceive. Appropriate quantities to express this bending rigidity will be given in the next chapter.

The lateral viscosity of lipid membranes in the L_α–phase was measured to be in the range of $0.1 - 1$ Pa·s [HLMZ77] which approximately equals the value for viscous oil [Kuc91]. Measurements are conducted by applying EMR or NMR to determine the rotational relaxation times of the lipids, which turns out to be about $10^{-7} - 10^{-8}$ s. Hence, a single molecule can travel as far as some microns per second. Diffusion coefficients for embedded proteins (see next section) can be measured by a method called FRAP *(Fluorescence Recovery After Photobleaching)*, where fluorescent marker proteins are (irreversibly) photobleached by an intense Laser pulse and the recovery time is measured, as particles are replaced by lateral diffusion and the bleached spot vanishes [Ack92].

I.4 Embedded Particles

As mentioned before, especially biological membranes host a large number of particles, which "float" in the ambient membrane. The lipid layers themselves promote embedding of foreign particles by developing gaps in "gtg-kinks", which are zig-zag-like deviations from the regular bilayer pattern [HLMZ77]. Even without this effect, complete absence of *co-surfactants* would be unfavorable due to entropy.

Especially proteins account for a large weight fraction in biomembranes (40-60%). *Integral* and *marginal* inclusions are being distinguished, depending on whether they span the membrane in its entire thickness or not. So-called "ion-pumps", e.g. in erythrozytes, can be giant molecules compared to the small lipids. Other impurities such as "gemini" (two lipids linked at their head groups forming some sort of horseshoe structure, see Fig. I.3) are less deviating in size. Inclusions can be isotropic (rotational invariant normal to the plane) or not. It has been shown that even small amounts of inclusions can alter membrane properties dramatically (see Fig. I.5). The complex interaction of these particles with each other and the membrane was, and will be later in this treatment, object of in-depth investigation.

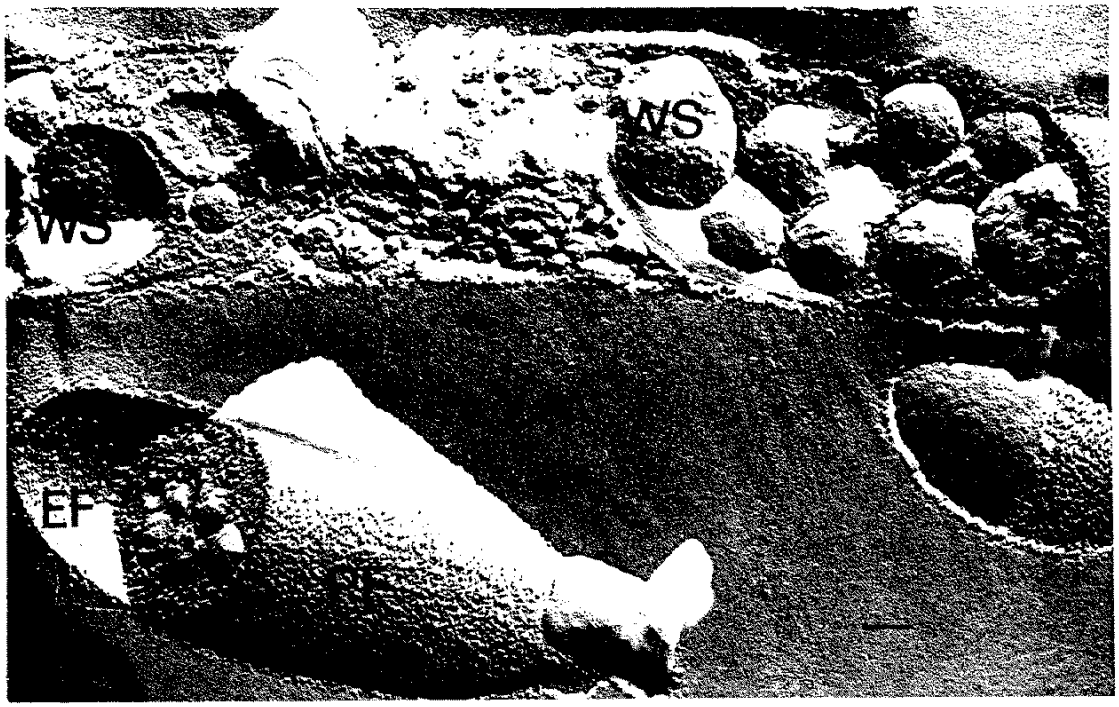

***Figure** I.5: Freeze-fracture cryo-TEM micrograph of cells of the bacterium Streptomyces hygroscopicus, taken from [SG87]. The area EF contains few protein particles, the other, right section of the fish-shaped structure has a high protein density. The areas WS show a raspberry-like wafer structure with bulges of 30-40 nm in size. The bar in the lower right corner represents 100 nm (about the width of the letter "W").*

To name one prominent example, the thermal *flicker-phenomenon* of erythrozytes (red blood cells), a quasi-periodic global shape fluctuation, is attributed to a combination of most of the effects summarized so far, stemming from both the pure membrane (bending rigidity, internal order parameters etc.) as well as inclusion interaction. In addition, there is a driving pressure difference between the in- and the outside of the vesicle (lower pressure inside).

II. Forces

II.1 Bending Hamiltonian

In this chapter, the elastomechanical properties of thin layers with bending rigidity but vanishing surface tension shall be discussed. Following the biological terminology, these will be called *membranes*, in distinction to *films* with finite surface tension (e.g. soap bubbles). However, in the theory of elasticity, the first kind is rather termed *elastic shell* [LL59], whereas films are called "membranes".

First, an expression for a bending energy density suitable for lipid membranes will be constructed from simple differential geometry and symmetry arguments. After a discussion of a few important mathematical properties, the Hamiltonian will be reviewed in terms of the theory of elasticity. In the end, the constants in the formulation will be compared to experimental data.

As mentioned before, lipid membranes show a bending energy density controlled by the local curvature. The remainder of this work will only deal with membranes whose curvature radii are large compared to their thickness. Obviously, the curvature energy of a shell cannot depend on its spatial orientation, i.e., the embedding in the surrounding space. Also, we assume that the membranes have indistinguishable upper and lower surfaces. Thus, the bending energy must be invariant with respect to rotations, translations and reflections of the coordinate system. Therefore, only the invariants of the curvature tensor b, denoted by $H := \mathrm{Tr}\ \mathsf{b} = c_1 + c_2$ and $K := \det\ \mathsf{b} = c_1\ c_2$ (see appendix A.1, eqns. (A.5a), (A.5b)) can be of importance for the Hamiltonian. Here, $c_{1,2}$ are the surface principal curvatures, H is *twice* the mean curvature ($H = c_1 + c_2$), and K the Gaussian curvature. Since H changes sign when the surface is turned upside down (reflected at a plane), only even powers of H can be part of a reasonable bending Hamiltonian. In contrast, K is bilinear in the curvatures and thus invariant with respect to reflections. With this input, we can find a bending energy density g to lowest order, first given by Canham in 1970 [Can70] and Helfrich in 1973 [Hel73]

$$\boxed{g = \frac{\kappa}{2}\,(c_1 + c_2)^2 + \bar{\kappa}\ c_1 c_2 = \frac{\kappa}{2}\,H^2 + \bar{\kappa}\,K} \quad . \tag{II.1}$$

The coefficients κ and $\bar{\kappa}$ are called, respectively, *bending modulus* and *Gaussian modulus*, and have the dimension of energy. It is assumed that curvature radii $R_1 \equiv 1/c_1, R_2 \equiv 1/c_2$ are always large compared to the membrane thickness, so higher powers such as $H^4, H^2K, K^2, (\nabla H)^2$ etc ... can be neglected here. (However, there have been different approaches [Goe93, Bal81]).

Also, a surface area dependent term was omitted, based on the experimental result that surface tension vanishes for lipid membranes [Isr92].

The total bending energy of a surface S given by $\boldsymbol{x}(u,v)$ can thus be written as

$$E_{\rm tot} = \int_S \Big(\frac{\kappa}{2}\,H^2 + \bar\kappa\,K\Big)\;{\rm d}A = \int_S \Big(\frac{\kappa}{2}\,H^2 + \bar\kappa\,K\Big)\,\sqrt{|\mathsf{g}|}\;{\rm d}u\,{\rm d}v \quad , \tag{II.2}$$

where ${\rm d}A$ denotes the surface area element and $|\mathsf{g}| \equiv \det \mathsf{g}$ is the determinant of the surface metric tensor, see eq. (A.2b).

Two important mathematical details can immediately be concluded:

- The Helfrich bending energy eq. (II.2) is scale independent. Scaling the surface by a factor $\boldsymbol{x} \to \alpha\,\boldsymbol{x}$ also scales the curvature radii $R \to \alpha\,R$, thus it acts inversely on the curvatures: $H^2 \to (H/\alpha)^2,\; K \to K/(\alpha^2)$. This change is compensated by the scaled integration measure ${\rm d}A \to \alpha^2\,{\rm d}A$.

- By virtue of the Gauß-Bonnet theorem [Spi70, Car83] (see appendix A.2), the identity

$$\int_S K\;{\rm d}A = 4\pi(1-\mathfrak{g}) \tag{II.3}$$

  holds, where $\mathfrak{g}$ is the "genus" of the surface ($\mathfrak{g} = 0$ for a vesicle). This equation will enable us later to omit the K-dependent term in $E_{\rm tot}$ from eq. (II.2), whenever only differences in bending energy rather than absolute values are of interest.

  Hence, eqns. (II.1),(II.2) reduce to the simple formulas

$$\boxed{g = \frac{\kappa}{2}\,H^2 \;+\; \text{const} \quad , \qquad E_{\rm tot} = \frac{\kappa}{2}\int_S H^2\;{\rm d}A \;+\; \text{const}} \tag{II.4}$$

  which is valid as long as the surface maintains constant topology, e.g. the surface cannot change its shape from a bubble to, say, a torus.

Sometimes [Hel73], the assumption of up-down symmetry is dropped and a *spontaneous curvature* c_0 is introduced to eq. (II.1) by

$$g = \frac{\kappa}{2}\,(c_1+c_2-c_0)^2 + \bar\kappa\,c_1c_2 = \frac{\kappa}{2}\,H^2 - \kappa\,c_0H + \bar\kappa\,K \quad . \tag{II.5}$$

However, consequences of this ansatz will not be pursued here.

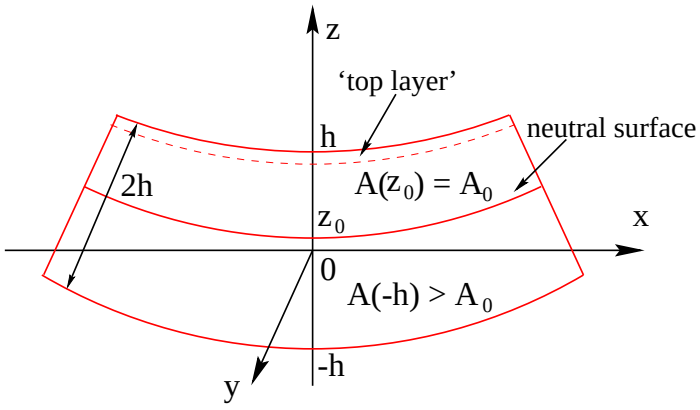

***Figure** II.1: Exaggerated sketch of a bent plate with $H > 0$. Upper layers are compressed, while lower layers are expanded. The neutral surface lies at $z = z_0$ which is not necessarily in the middle of the plate. The difference between $A(z)$ and $A_0 = A(z_0)$ determines $\delta A := (A(z) - A_0)/A_0$ (see eq. (II.6)).*

II.2 Bending Coefficients

The dependence of the coefficients κ, $\bar{\kappa}$ on microscopic properties of the shell are discussed in this section. To start, we imagine the shell as a plate of thickness $2h$, where h is supposed to be small compared to its lateral extent. The plate may be laterally homogeneous and isotropic. It is assumed to be flat in the ground state. In (Fig. II.1), it is shown as bent along the y-axis. The plate may be thought of as divided into an imaginary stack of "layers" oriented parallel to its surface. It is clear, without any assumption about the inner structure, that layers close to the convex side of the plate will be stretched, while layers close to the concave side (upper side in the figure) are compressed. Both deformations cost energy and are the microscopic reason for the Helfrich bending energy eqns. (II.1),(II.2). This energy depends on the change in surface area of the corresponding layer inflicted by the bending. Somewhere in the inside of the plate lies the "neutral surface" whose surface area remains constant [LL59], the position of this layer is denoted by z_0 (not necessarily in the middle). The relative change in surface area at z is given by [Goe93]

$$\delta A(z) := \frac{A(z) - A_0}{A_0} = -(z - z_0)H + (z - z_0)^2 K \quad , \tag{II.6}$$

for a proof, see appendix A.3 .

The Taylor expansion of the *volume* elastic energy density in a layer around the equilibrium state is to second order

$$\begin{aligned} g_{\mathrm{Vol}}(z) &= \frac{\partial\, g_{\mathrm{Vol}}}{\partial\, \delta A}\Big|_{\delta A=0} \delta A(z) + \frac{1}{2}\, \frac{\partial^2 g_{\mathrm{Vol}}}{\partial (\delta A)^2}\Big|_{\delta A=0} (\delta A(z))^2 \\ &= s(z)\, \delta A(z) + \frac{k_a(z)}{2}\, (\delta A(z))^2 \quad , \end{aligned} \tag{II.7}$$

where $s(z)$ is the lateral stress in the plate. If $s(z) \equiv 0$, eq. (II.7) is analogous to Hooke's law.

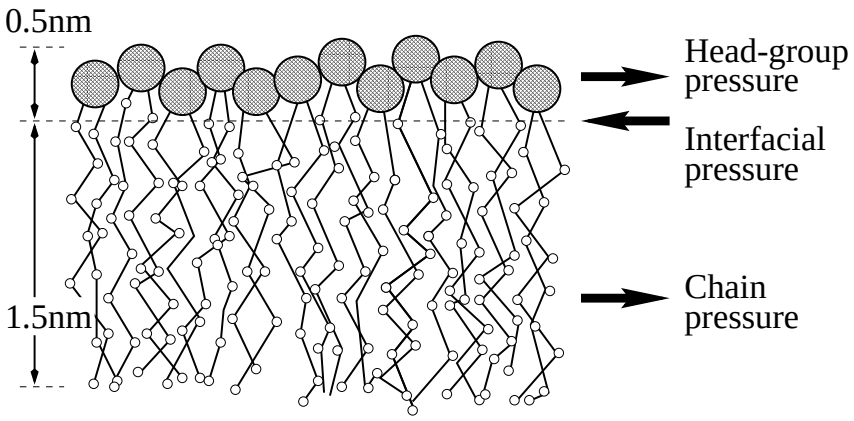

***Figure** II.2: Lipid monolayer with double-chained amphiphiles; both heads and tail chains repel each other. The "head groups" themselves contain 10-40 atoms (Adapted from [Isr92]).*

However, even for the flat bilayer, $s(z)$ does in general not vanish. Equilibrium stress distribution in lipid membranes is not simple and different models were proposed: Tail chains are either believed to attract each other (S. Leibler in [NPW89]), or are also thought to be mutually repulsive and attraction is constrained only to an interfacial layer between these two parts [Isr92], see Fig. II.2. Adjacent head groups repel each other due to their electric charge in all models. Substituting eq. (II.6) into eq. (II.7) and omitting curvature terms beyond quadratic order, we find (with the shorthand $\Delta z := (z - z_0)$)

$$g = \int_{-h}^{h} g_{Vol} \, \mathrm{d}z \tag{II.8}$$

$$= \int_{-h}^{h} \frac{k_a}{2} (\Delta z)^2 \, H^2 - s(z) \, \Delta z \, H + s(z) \, (\Delta z)^2 \, K \quad \mathrm{d}z \quad . \tag{II.9}$$

This can be compared with eq. (II.5) to identify corresponding terms:

$$\kappa = \int_{-h}^{h} \frac{k_a(z)}{2} \, (\Delta z)^2 \, \mathrm{d}z \tag{II.10a}$$

$$\bar{\kappa} = \int_{-h}^{h} s(z) \, (\Delta z)^2 \, \mathrm{d}z \tag{II.10b}$$

$$\kappa \, c_0 = -\int_{-h}^{h} s(z) \, \Delta z \, \mathrm{d}z \quad . \tag{II.10c}$$

Eq. (II.10c) is of no further interest since it corresponds to spontaneous curvature which we assumed to vanish.

For a homogeneous plate, one would expect $z_0 = 0$ and both constant $s(z) = s$ and constant stretching modulus distribution $k_a(z) = k_a = \mathrm{const}$. Substituting this in eqns. (II.10a) and

(II.10b), we end up with

$$\kappa = k_a \frac{1}{3} h^3 \tag{II.11a}$$

$$\bar{\kappa} = s \frac{2}{3} h^3 \quad . \tag{II.11b}$$

These results can be compared to the standard theory of elasticity of a thin, homogeneous plate in equilibrium [LL59]

$$g = \underbrace{\frac{E\, h^3}{3(1-\mu^2)}}_{=\kappa/2} H^2 + \underbrace{\frac{2E\, h^3}{3(1+\mu)}}_{=\bar{\kappa}} K \quad , \tag{II.12}$$

where E is the elastic modulus and μ Poisson's ratio of the plate ($\mu \in [0,\, 0.5]$ for all known materials). The coefficients can now be identified with, respectively, $\kappa/2$ and $\bar{\kappa}$.

It is worth pointing out that $\kappa, \bar{\kappa}$ only depend on h to third order for constant k_a. If, however, the stretching modulus vanishes everywhere except for small regions $d \ll h$, the integration eq. (II.8) rather yields a quadratic dependence in h. In realistic models, a relationship $\kappa, \bar{\kappa} \propto h^\eta$ with $2 < \eta < 3$ is expected (S. Leibler in [NPW89]).

II.3 Microscopic Physics of Lipid Membranes

Lipid molecules can form aggregates that have the strange feature of being fluid-like. This is due to the weakness of the forces that bind them together, which are Van-der-Waals, hydrophobic, hydrogen-bond, and screened electrostatic forces, but do not include strong ionic or covalent forces. Unsaturated carbon atoms in the chains increase fluidity [Isr92].

Depending on the type of lipids, the ambient solvent, temperature, and presence of ions (solved salts etc.), lipid molecules can form a variety of aggregates as discussed in chapter I. The type of preferred aggregate shape depends very much on the form of the lipids. If the molecules are cone-shaped, i.e. they have big head groups and slim chains, they rather form highly curved objects such as micelles. Conversely, if head groups are small and tail chains bulky, bilayers are assumed. In fact, most of the bilayer amphiphiles have two tail chains (see Fig. I.1), which gives them a more cylindrical or truncated cone shape [Isr92, HLMZ77]. The critical quantity is the *packing parameter* $v/A_h l_c$ (v, A_h, l_c : molecular volume, headgroup area, total length), see Fig. II.3. Values of $v/A_h l_c < 1/2$ give micelles, $1/2 \ldots 1$ bilayers and $v/A_h l_c > 1$ can form "inverted micelles" where headgroups are directed towards the micelle interior and tails outside [Isr92].

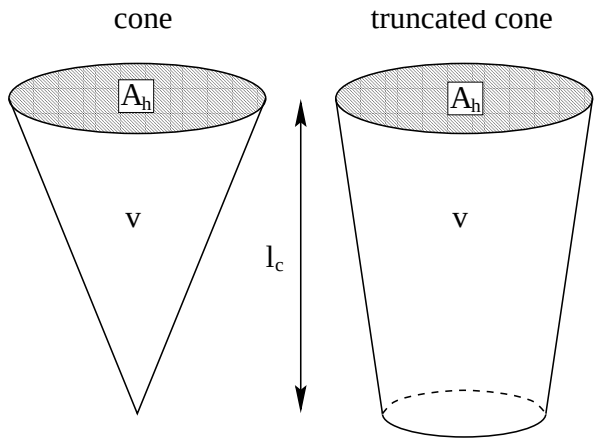

***Figure** II.3: Critical packing shapes cone ($v/A_h l_c < 1/3$) and truncated cone ($1/3 < v/A_h l_c < 1/2$)*

Some other characteristic mechanical properties:

- There is an optimal surface area per molecule (head group) A_h, corresponding to eq. (II.7). The stretching energy is harmonic around A_h:

$$E_S(A_h) = \frac{k_A}{2} \frac{(A_h - A_{h,0})^2}{A_h} + O({A_h}^3) \tag{II.13}$$

  with values of $k_A = 100 \ldots 230$ mJ·m^2, [Isr92]. However, the membrane tears if stretched beyond $(A_h - A_{h,0})/A_h \approx 1\%$ [Lip98].

- Measured values for κ in bilayers lie in the range $2 \ldots 20 \times 10^{-20}$ J $= 5 \ldots 50\ k_{\mathrm{B}}T$ at room temperature and about half as much for monolayers [Isr92, HLMZ77]. Therefore, lipid membranes are "soft matter" systems, where typical energies range around $k_{\mathrm{B}}T$. The Gaussian modulus $\bar{\kappa}$ is hard to measure, since changes in membrane topology would be required. However, there have been recent approaches to numerically simulate fluid membranes in the sponge phase, where $\mathfrak{g} \propto V$ [GK98] and thereby determine $\bar{\kappa}$.

- The lipid membrane volume compressibility, in which the membrane material is treated as a bulk fluid

$$K_B = -\frac{1}{V} \left(\frac{\partial V}{\partial P} \right)_T \tag{II.14}$$

  with values of some $K_B \approx 10^{-9}\ 1/\mathrm{Pa}$ is comparable to that of water ($0.5 \times 10^{-9}\ 1/\mathrm{Pa}$, [Kuc91]), which is almost incompressible. Thus, stretching the total membrane area is directly linked to a change in thickness (Poisson's ratio is $\mu = 1/2$). This further supports the notion of treating a lipid membrane as a 2D-fluid.

III. Fluctuations

III.1 Elementary Thermodynamics of Fluid Membranes

The last chapters dealt with the microscopic and deterministic properties of fluid membranes. This chapter will extend the discussion to thermodynamical aspects and fluctuations. These are crucial to define characteristic lengths on fluctuating surfaces and later to determine interactions between surface particles.

First, a more precise discussion of *surface tension* is in order. A 2-dimensional surface in 3-dimensional space has a surface area A. If it is framed (such as a soap film in a wire loop) or fluctuates around an ideal shape (a soap bubble, lipid vesicle, or a tube-like structure), also a *projected area* A_p can be defined (the area of the wire loop, surface of the ideal sphere/tube etc.), where $A \geq A_p$. These two surfaces areas are independent thermodynamical variables [DL91] and pertain to two conjugate surface tensions, respectively, σ and σ_p. Therefore, in keeping two of these four quantities constant, we can define four different thermodynamic ensembles, listed in the following table [DL91]:

(i)	(A, A_p)	isolated, framed
(ii)	(A, σ_p)	isolated, unframed
(iii)	(σ, A_p)	open, framed
(iv)	(σ, σ_p)	open, unframed

The first two ensembles are called isolated, since the total surface area (and therefore the total number of surface molecules, see chapter II) is kept constant. A thermodynamical potential can be assigned to each of these ensembles [DL91].

When stating that lipid membranes have no surface tension, it is meant that σ vanishes for some finite value of A. This behavior is opposite to that of a soap bubble, in which surface tension has its minimum for $A \rightarrow$ (soap bubbles are stabilized against deflation only by internal pressure). In contrast, σ_p is controlled by the bending stiffness κ and the temperature T and vanishes at some finite value of A_p.

III.2 Persistence Length

Fluctuating polymers and surfaces with finite bending stiffness are locally smooth, but the orientation correlation decays over long length scales (S. Leibler in [NPW89], [MM94, GK97b, Pel86]). The characteristic length which separates the two scales is called *persistence length*

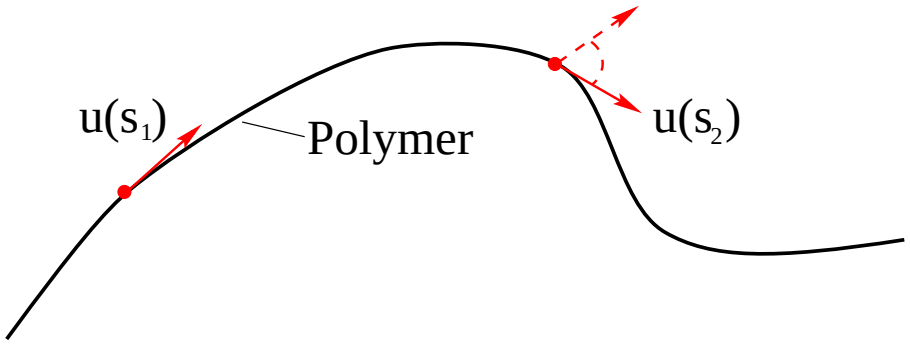

***Figure** III.1: Curved linear polymer. The correlation of the tangential vector decays on average exponentially along the contour length.*

ξ_P. The definition can be illustrated on a linear polymer of length L in 3-D space, given by the function $\mathbf{r}(s)$ along its contour length s. For a finite bending stiffness κ_P, the bending energy of the polymer is given in the Kratky-Porod model [DE86] by

$$U_{\text{bend}} = \frac{\kappa_P}{2} \int_0^L \left(\frac{\partial \mathbf{u}}{\partial s} \right) \, \mathrm{d}s \; , \tag{III.1}$$

where $\mathbf{u}$ is a unit tangential vector to the chain $\mathbf{u}(s) = \partial \mathbf{R}/\partial s$ (Fig. III.1). The equilibrium conformational distribution of the polymer (the probability to find it in the state $\mathbf{r}(s)$) is given by the Boltzmann distribution

$$\Psi[\mathbf{r}] = \exp\left(-\frac{U_{\text{bend}}}{k_{\text{B}} T} \right) \quad , \tag{III.2}$$

where $k_{\text{B}} = 1.38 \times 10^{-23}$ J/K is Boltzmann's constant. Eqns. (III.1) and (III.2) describe a Gaussian diffusion process. [1] The tangential vector correlation function is thus known to be

$$\nu_P(s) := \Big\langle \mathbf{u}(s_0) \cdot \mathbf{u}(s_0 + s) \Big\rangle_{s_0} = \exp\left(-\frac{|s|}{\xi_P} \right) \; , \tag{III.3}$$

$$\text{with (for the Gaussian case)} \qquad \xi_P = \frac{\kappa_P}{k_{\text{B}} T} \quad . \tag{III.4}$$

Note that eq. (III.4) is not a definition but the special result for the Gaussian case. Two parts of a polymer which are separated by a contour length s larger than ξ_P are uncorrelated in orientation.

In principle, eq. (III.3) can be generalized to surfaces by replacing the tangential vectors by the surface normal $\mathbf{n}(\boldsymbol{x})$

$$\nu(\ell) := \Big\langle \, \mathbf{n}(\boldsymbol{x}_1) \cdot \mathbf{n}(\boldsymbol{x}_2) \, \Big\rangle_{\ell = \overline{\boldsymbol{x}_1, \boldsymbol{x}_2}} \quad , \tag{III.5}$$

[1] The tangential vector $\mathbf{u}(s)$ along the contour length s formally equals the time evolution of a vector quantity under rotational Brownian motion $\mathbf{u}(t)$ ($\|\mathbf{u}\| = 1$ in both cases) [DE86]. The persistence length is therefore equivalent to an inverse temporal diffusion constant ($\xi_P \mathrel{\widehat{=}} 1/(2D_r)$)

where the average is taken over all pairs of points $(\boldsymbol{x}_1, \boldsymbol{x}_2)$ on the surface, whose shortest geodesic distance is ℓ. However, a regular 2-D surface in 3-D space has, similar to a 1-D polymer in 2-D space, stronger geometrical constraints so that self-avoidance and continuity conditions become more important. Especially if a membrane is framed or has fixed topology (e.g., a closed surface), the normal-normal correlation cannot always be expected to decay to zero. However, there are alternative definitions of the persistence length, which will be discussed below. The persistence length will become important when for instance surface particle interaction is treated in chapters V and VI.

III.3 Scaling

To further illustrate the importance of the number of dimensions and self-avoidance, the scaling behaviors of a D-dimensional network of Hookean springs ($D = 1$: linear chain, $D = 2$: "membrane") embedded in d-dimensional space are compared. No bending stiffness is assumed here. Let L be the linear size of the network (e.g. the chain contour length, the diameter of the stretched membrane etc.) and $R \ \ (\leq L)$ its size in space (e.g. $R = R_g$ radius of gyration, see eq. (V.5)). Then L and R are related by [DE86, GK97b]

$$R \propto L^{\omega} \quad , \qquad \omega := \frac{D+2}{d+2} \tag{III.6}$$

for self-avoiding and

$$R \propto \begin{cases} L^{(2-D)/2} & \text{for } \ D < 2, \\ \sqrt{\ln(L)} & \text{for } \ D = 2 \end{cases} \tag{III.7}$$

for non-self-avoiding (self-intersecting or so-called *phantom*) networks. Eq. (III.6) is known as the Flory estimate, while (III.7) is an exact result (random walk). For $d = 3$ and polymers ($D = 1$), we get respectively $L^{3/5}$ and $L^{1/2}$, and for membranes ($D = 2$), we get $L^{4/5}$ and $\sqrt{\ln(L)}$ (Note that the phantom result is not algebraic!).

The class of structures which scales like eqns. (III.6), (III.7) is called *crumpled* networks. This scaling type is *fractal* [Man87], as the ratio of volume to surface area of a closed crumpled surface is negligible compared to that of a body with a smooth surface in the mathematical sense (e.g. a sphere):

$$\frac{V}{A} \propto \frac{R^3}{L^2} \ \propto \begin{cases} L^3/L^2 = L & \text{for smooth bodies,} \\ L^{3\omega}/L^2 = L^{2/5} & \text{for crumpled bodies } (D = 2, \ d = 3) \end{cases} . \tag{III.8}$$

According to recent results [GK98, IJ95], even membranes with finite bending stiffness are always in the crumpled phase. In other words, for diverging membrane sizes, the spatial extent of

lipid membranes compared to smooth bodies becomes negligible. [2] Therefore, for finite bending stiffness, a scaling crossover

$$\frac{\langle V\rangle}{\langle A\rangle^{3/2}} \propto \frac{\langle V\rangle}{L^3} = \Theta\big(L/\xi_M\big) \tag{III.9}$$

can be expected [IJ95, GK96], where a rigid and a flaccid regime meet at lengths close to the persistence length. Θ must obey $\Theta(x) \approx$ const in the rigid regime where $L \ll \xi_M \quad (x \ll 1)$ and $\Theta(x) \propto x^{-1}$ in the flaccid regime with $L \geq \xi_M$ (large x). [The latter case is called ***branched polymer*** scaling; the Flory estimate would give the slightly different result of $\Theta(x) \propto x^{-3/5}$.] Eq. (III.9) will be used in chapter VI.

III.4 Spherical Fluctuations

As stated earlier, lipid vesicles are similar to bubbles fluctuating around a spherical shape. Therefore, it is reasonable to expand eq. (II.4) into (normalized, complex) spherical harmonics [Hel86, MS87, MM94, GK96, GK97b], which form a complete orthonormal system in $\mathcal{L}_2(S^2)$ [Wla72] with

$$Y_l^m(\vartheta,\phi) \;:=\; \eta_l^m \; P_l^{|m|}(\cos\vartheta) \;\; \mathrm{e}^{i\,m\phi} \quad , \qquad l = 0,\,1,\,2,\ldots \;; \quad -l \leq m \leq l \tag{III.10}$$

$$\int_{S^2} Y_l^m \left(Y_{l'}^{m'}\right)^* \,\mathrm{d}\Omega = \delta_{ll'}\,\delta_{mm'} \quad , \qquad (Y_l^m)^* \equiv Y_l^{-m} \qquad . \tag{III.11}$$

The $P_l^m(\cdot)$ are the associated Legendre polynomials, η_l^m are (real) normalizing factors, δ_{ab} is Kronecker's delta, and the asterisk * denotes complex conjugation. Spherical harmonics are the eigenbase of the Laplacian Δ_{S^2} on the sphere S^2 (also called Beltrami's operator [Wla72])

$$\Delta_{S^2} Y_l^m \;=\; q_l\, Y_l^m \,, \qquad q_l = -l(l+1) \tag{III.12}$$

$$\Delta_{S^2} \;=\; -\frac{1}{\sin\vartheta}\,\frac{\partial}{\partial\vartheta}\left(\sin\vartheta\,\frac{\partial}{\partial\vartheta}\right) - \frac{1}{\sin^2\vartheta}\,\frac{\partial^2}{\partial\phi^2} \quad , \tag{III.13}$$

with the eigenvalues q_l. The vesicle shape can be expressed as a normalized radial height field $h(\vartheta,\phi)$ over the sphere of radius R_0

$$r(\vartheta,\phi) \;=\; R_0\big[1 + h(\vartheta,\phi)\big] \quad , \tag{III.14}$$

and expanded in spherical harmonics

$$h(\vartheta,\phi) \;=\; \sum_{l=0}^{l_M} \sum_{m=-l}^{l} a_l^m \; Y_l^m(\vartheta,\phi) \quad , \tag{III.15}$$

[2] However, for $d > 5,\ D > 4$, there is a so-called ***flat phase*** which scales non-fractally and, with decreasing bending stiffness, a *crumpling transition* to the crumpled phase [GK96] is encountered

where $(a_l^m)^* = a_l^{-m}$, since the height field is real. The summation limit l_M is a large wavenumber cutoff determined by the conformational number of degrees of freedom f. This cutoff is given for a lipid membrane by a microscopic length a (vesicle head diameter) and in simulations by the bond lengths (see next chapter). Since only lateral oscillations are of interest here, the number of degrees of freedom approximately equals N

$$f = (l_M + 1)^2 = N \quad , \tag{III.16}$$

[GK96, Hel86]. However, a more exact determination of f would involve a discussion of how many vertices are at least necessary to unambiguously "sample" all Y_l^m up to a certain $l = l_M$.

Using eq. (III.15), we can express the Helfrich bending energy eq. (II.4) to order h^2 as [GK96]

$$\boxed{E = \frac{\kappa}{2}\int H^2 \ \mathrm{d}A = 8\pi\kappa + \frac{\kappa}{2}\sum_{l\geq 2}^{l_M}\sum_{m=-l}^{l}\big[q_l(q_l+2)\big]\ |a_l^m|^2} \quad . \tag{III.17}$$

Spherical harmonics with $l < 2$ do not contribute since they just correspond, respectively, to changes in the membrane area and overall translations. Note also that the energy does not depend on m ("magnetic quantum number"). $8\pi\kappa$ is the curvature energy for a perfect sphere and thus the minimal or ground state energy. Hence, the double sum in eq. (III.17) represents the excess bending energy due to corrugations.

By virtue of eq. (III.12), eq. (III.17) shows no mode coupling; the Helfrich Hamiltonian on the sphere becomes diagonal. Eq. (III.17) can therefore be combined with the equipartition theorem ($k_\mathrm{B}T/2$ on average per degree of freedom) to yield expectation values of the total bending energy of

$$\langle E\rangle = 8\pi\,\kappa + \frac{f}{2}\,k_\mathrm{B}T \tag{III.18}$$

and of the magnitude of each spherical harmonic of

$$\langle|a_l^m|^2\rangle = \frac{k_\mathrm{B}T}{\kappa\big[q_l(q_l+2)\big]} \quad \propto \quad l^{-4} \quad . \tag{III.19}$$

Again, the last result is independent of m in this approximation.

A term similar to eq. (III.17) can be found for the volume of the vesicle [GK96]

$$\frac{V}{V_0} = 1 + \frac{3}{8\pi}\sum_{l\geq 2}^{l_M}\sum_{m=-l}^{l}\left(1+\frac{q_l}{2}\right)\ |a_l^m|^2 \quad , \tag{III.20}$$

where $V_0 := (4/3)\pi\ {R_0}^3$ is the volume of the ground state sphere (see definition in chapter VI, pg. 39). Combining eq. (III.20) with eq. (III.19), and keeping in mind that $2l+1$ spherical

harmonics pertain to each l, one obtains

$$\begin{aligned}\frac{\langle V\rangle}{V_0}-1 &= \frac{3k_{\mathrm{B}}T}{8\pi\kappa}\sum_{l\geq 2}^{l_M}\frac{(2l+1)(1+q_l/2)}{q_l(q_l+2)} = -\frac{3k_{\mathrm{B}}T}{8\pi\kappa}\sum_{l\geq 2}^{l_M}\frac{2l+1}{2l(l+2)} \\ &\approx -\frac{3k_{\mathrm{B}}T}{8\pi\kappa}\int_2^{l_M}\frac{\mathrm{d}l}{l} = -\frac{3k_{\mathrm{B}}T}{8\pi\kappa}\ln(l_M/2) \end{aligned} \tag{III.21}$$

for the expectation value of the relative change in volume $(\langle V\rangle / V_0)-1$. A similar formula holds for the radius of gyration R_g [GK97b]

$$\frac{\langle R_g\rangle}{R_0}-1 = -\frac{k_{\mathrm{B}}T}{4\pi\kappa}\ln(l_M/2) \quad . \tag{III.22}$$

Eq. (III.21) is scale-dependent. Therefore, a renormalized, distance dependent bending rigidity $\kappa_R(\ell)$ can be defined which (approximately) follows $(\langle V\rangle\ /\ V_0) - 1 \propto -1/\kappa_R + O({\kappa_R}^{-2})$. In the limit $\ell \searrow a$, κ_R should equal κ, while at lengths close to the membrane persistence length ($\ell \nearrow \xi_M$), κ_R should vanish:

$$\kappa_R(\ell) := \kappa - \frac{3k_{\mathrm{B}}T}{4\pi}\ln(\ell/a_0) \quad , \tag{III.23}$$

where a is the microscopic cut-off length [GT82, PL85, Hel85, Hel86, För86, Kle86, DL91, Mor94, GK96]. Eq. (III.23) can be interpreted as a *thermal softening* of the bending rigidity: It is easier to bend a membrane which already contains some ripples. Conversely, the assumption that $\kappa_R(\ell)$ vanishes at $\ell \approx \xi_M$ serves as an alternative, phenomenological definition of the persistence length in membranes:

$$\xi_M = a\ \exp\left(\frac{4\pi}{3}\frac{\kappa}{k_{\mathrm{B}}T}\right) \quad , \tag{III.24}$$

where ξ_M depends much stronger on κ than ξ_P in eq. (III.4).

Membrane softening can also be understood as a result of an increase in entropy ΔS [Hel86]

$$\Delta S = k_{\mathrm{B}}\ \ln(f) = 2k_{\mathrm{B}}\ \ln(l_M+1) \quad , \tag{III.25}$$

due to the additional degrees of freedom.

Note that eq. (III.21), eq. (III.22), and thus eq. (III.23), are only valid for small corrugations $h \ll R_0$ which is the case for stiff membranes ($\kappa/k_{\mathrm{B}}T \gg 1$). Also, the latter equations are not valid anymore in the presence of additional constraints such as constant volume V [Hei97] and/or surface area A [Kra96]. Especially the assumption of constant volume might be realistic in many biophysical applications, if lipid vesicles are filled with an incompressible fluid.

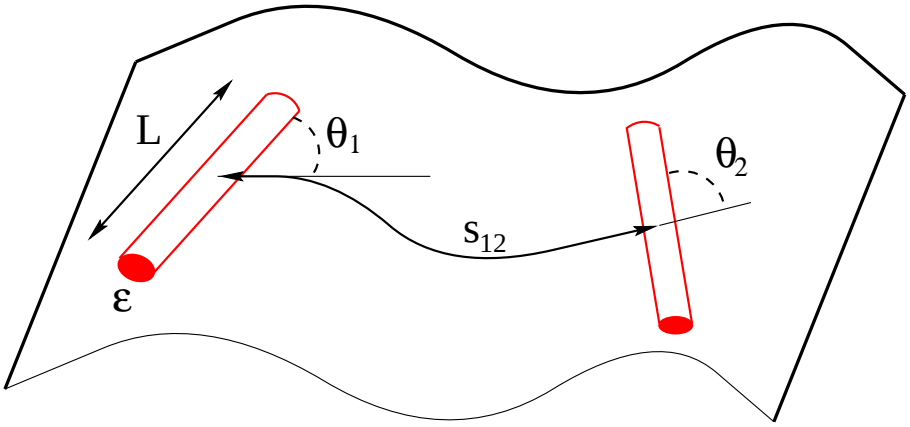

***Figure** III.2: Curved membrane patch with two rod-like inclusions of length L and width $\epsilon \ll L$ separated by the geodesic line s_{12} of length s. The two rods are rotated by the angles θ_1, θ_2 (in the tangential plane) against s_{12}. All rods are assumed to be equal.*

III.5 Surface Particles

While there has been extensive research completed on the microscopical and thermodynamical behavior of lipid membranes (or, in mathematical terminology, D-dimensional manifolds in d-dimensional space), only a small fraction of the work has been devoted to the interaction of *surface inclusions* (i.e., particles different from lipid molecules which can or cannot freely translate within the fluid membrane, see chapter I).

There are a few analytical investigations, some of which [Fou96, Hol97] focus on inclusion/membrane interaction and others on inclusion/inclusion interaction for *isotropic* (round cross-section along the membrane plane) [GBP93, Fou96, PL96, Fou97, WKH98] or *anisotropic*, rod-like inclusions [GGK96a, GGK96b, PL96]. The latter group is of special interest, since part of the Monte-Carlo simulation described later deals with anisotropic surface inclusions. Inclusion/inclusion interaction can be split up into *direct* (electrostatic and Van-der-Waals) forces and *indirect* forces, which are mediated by membrane fluctuations. Indirect forces will be of special interest in the simulation.

In [GBP93], isotropic (round) inclusions with area $A_{\text{inc}} = \pi(L/2)^2$ are assumed and an interaction potential Φ_{RR} of

$$\Phi_{\text{RR}}(s) = -k_{\text{B}}T \, \frac{12 A_{\text{inc}}^2}{\pi^2 s^4} + \text{O}(1/s^6) \tag{III.26}$$

is found ([Par96] only compute $\Phi_{\text{RR}}(s)$ as half as strong).

In [GGK96a, GGK96b], slim rods of length L as illustrated in Fig. III.2 are assumed and a result of

$$\Phi_{\text{RR}}(s, \theta_1, \theta_2) = -\frac{k_{\text{B}}T}{128} \left(\frac{L}{s}\right)^4 \cos^2\big[2(\theta_1 + \theta_2)\big] + \text{O}(1/s^6) \tag{III.27}$$

is given, where $\theta_1,\ \theta_2$ are the rotational angles with the (shortest) connecting geodesic line s_{12}, see Fig. III.2. Hence, both contributions show the existence of an attractive interaction potential that falls off with distance as $(1/s)^4$ to leading order in $1/s$. This is only valid in the case $\xi_M \gg s \gg L$ and for infinitely rigid rods . The angular dependence of eq. (III.27) is the square of a quadrupole-quadrupole interaction in two dimensions and shows the counterintuitive property of being minimal (maximally attractive) for both parallel and perpendicular mutual orientation of the rods [GGK96a, GGK96b]. [3]

The s^{-4}-dependence in eqns. (III.26),(III.27) was verified by [PL96] with different methods such as field-theoretic approaches for many similar cases (isotropic/anisotropic incl., proteins etc.) which preserve up-down symmetry in the membrane. On long length scales, this attractive potential dominates over Van-der-Waals ($\Phi_{\mathrm{VdW}} \propto -s^{-6}$) and is caused by the ambient membrane, which can reduce the additional conformational constraints imposed by the immersed rods (membrane fluctuations vanish on the inclusion boundaries) for certain rod-rod positions such as parallel orientation. In other words, the membrane entropy is a function of inclusion distribution and thus some conformations are more favorable than others. This entropic attraction is the statistical mechanics equivalent of the quantum-mechanical *Casimir* [Cas48] effect, which describes e.g. the mutual attraction of two uncharged, conducting plates in vacuum due to vacuum fluctuations between them. With a separation distance s and plate area A_{pl}, the potential is $\Phi_{\mathrm{Casimir}} = -\hbar c\,(\pi^2/720)\,(A_{\mathrm{pl}}/s^3)$ [Cas48, KG97] (the different power s^{-3} is due to assuming 2-D plates as opposed to 1-D rods).

In conclusion, the problem connected to eqns. (III.26),(III.27) is that it just holds for rod-rod distances $s \gg L$. For smaller separations, analytical calculations are very hard to do. Given the total magnitude of $\Phi \ll k_{\mathrm{B}}T/128$ in eq. (III.27) which is two orders of magnitude smaller than the thermal energy $k_{\mathrm{B}}T$, it seems intriguing to find the short-range interaction for distances $s \lesssim L$, taking into account mutual rod-rod avoidance.

[3] It might seem strange that the interaction potential depends on the angle *sum* $\theta_1 + \theta_2$ in eq. (III.27), rather than the angle difference. See also the comment in the end of chapter V, pg. 42.

IV. Simulation

The Monte Carlo integration method will be discussed in this chapter from the mathematical point of view, followed by a section on surface and curvature discretizations.

IV.1 Monte Carlo Simulation

In order to find the *thermal average* $\langle\cdot\rangle$ of a quantity $\mathcal{A}$ for a certain thermodynamic ensemble, we have to integrate that quantity, weighted by the corresponding probability distribution function (PDF) over phase space. For the case of the canonical ensemble, this is simply the Boltzmann probability [AT87]

$$\langle\mathcal{A}\rangle_{\mathrm{NVT}} = \int_{\Gamma}\mathcal{A}(\boldsymbol{x})\ \rho_{\mathrm{NVT}}(\boldsymbol{x})\ \mathrm{d}\boldsymbol{x} \tag{IV.1}$$

$$\rho_{\mathrm{NVT}}(\boldsymbol{x}) := \frac{\exp\bigl(-\beta\,\Phi(\boldsymbol{x})\bigr)}{\int_{\Gamma}\exp\bigl(-\beta\,\Phi(\boldsymbol{x})\bigr)\ \mathrm{d}\boldsymbol{x}}\quad , \tag{IV.2}$$

where $\beta \equiv 1/k_{\mathrm{B}}T$ is the inverse temperature and $\langle\ \cdot\ \rangle_{\mathrm{NVT}}$ denotes the thermal average with respect to the const-NVT-ensemble (NVT: particle number, volume, and temperature).

Typical numerical integration methods such as Simpson's rule are no practical means to solve eq. (IV.1), since the phase space Γ can easily reach some hundred dimensions (e.g. for 100 point-like particles, the configurational part of the phase space alone has $d = 300$ dimensions). The efficiency of these deterministic integration techniques decreases rapidly with the number of dimensions because of the order of 10^d function evaluations are needed [AT87]. A better method is the random sampling algorithm, where N random points $\boldsymbol{x}_i \in \Gamma$ are chosen and eq. (IV.1) is replaced by a sum

$$\langle\mathcal{A}\rangle_{\rho} = \int_{\Gamma}\mathcal{A}(\boldsymbol{x})\ \rho(\boldsymbol{x})\ \mathrm{d}\boldsymbol{x} = \lim_{N\to\infty}\frac{\sum_i^N \mathcal{A}(\boldsymbol{x}_i)\ \rho(\boldsymbol{x}_i)}{\sum_i^N \rho(\boldsymbol{x}_i)} = \lim_{N\to\infty}\frac{|\Gamma|}{N}\sum_i^N \mathcal{A}(\boldsymbol{x}_i)\ \rho(\boldsymbol{x}_i) \tag{IV.3}$$

with $|\Gamma| := \int_{\Gamma}\mathrm{d}\boldsymbol{x}$. Although random sampling is by far more efficient than deterministic procedures, it can yet be improved, especially in the cases where the integrand $\mathcal{A}(\boldsymbol{x})\ \rho(\boldsymbol{x})$ in eq. (IV.3) almost only contributes in a small part of the phase space and is close to zero at all others (see Fig. IV.1). This is often the case in statistical mechanics, when the quantity $\mathcal{A}(\boldsymbol{x})$ varies slowly compared to the exponential PDF $\rho(\boldsymbol{x})$, eq. (IV.2). The remedy is to employ *importance sampling* by visiting some parts of the range of integration more often than others. When choosing

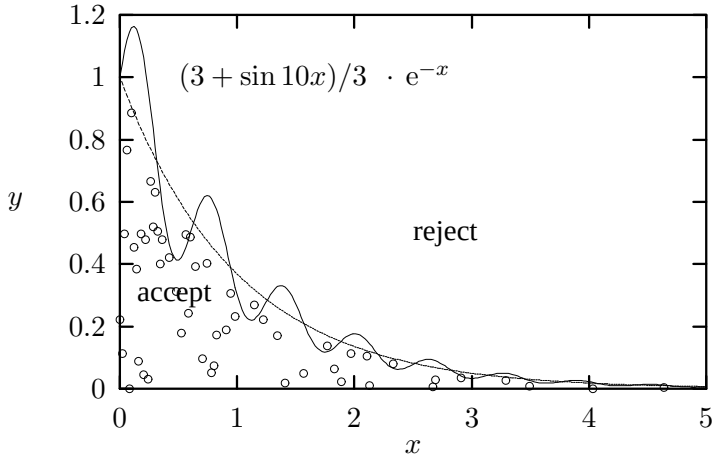

***Figure** IV.1: Importance sampling: For integrals such as $\int_0^5 (3+\sin 10x)/3 \cdot \mathrm{e}^{-x}\ \mathrm{d}x$, where the integrand is "concentrated" in some part of the integration domain, it is far more efficient to pick the sample points with a non-uniform probability (here e.g. e^{-x}). In the above plot, random points (x_i, y_i) within the bounding box could be chosen. The points which satisfy $y_i < \mathrm{e}^{-x_i}$ are "accepted", all others discarded, as sketched by the small circles under the dashed curve. The sum $(5/N_{\mathrm{accept}})\ \sum(3+\sin 10x_{i,\,\mathrm{accept}})/3$ then approximates the integral, see eq.* (IV.5).

the sample points from a PDF $\rho_{\mathrm{IS}}(\boldsymbol{x})$, eq. (IV.1) must be rewritten as

$$\langle \mathcal{A} \rangle_\rho = \int_\Gamma \mathcal{A}(\boldsymbol{x})\ \rho(\boldsymbol{x})\ \mathrm{d}\boldsymbol{x} = \int_\Gamma \left(\frac{\mathcal{A}(\boldsymbol{x})\ \rho(\boldsymbol{x})}{\rho_{\mathrm{IS}}(\boldsymbol{x})} \right)\ \rho_{\mathrm{IS}}(\boldsymbol{x})\ \mathrm{d}\boldsymbol{x} \quad , \tag{IV.4}$$

where the choice $\rho_{\mathrm{IS}} = \rho$ is most efficient. To approximate eq. (IV.4) by a sum, new random points $\tilde{\boldsymbol{x}}_i \in \Gamma$ are chosen which are not uniformly distributed, but with the probability $\rho(\tilde{\boldsymbol{x}}_i)$. In this case, eq. (IV.3) just becomes a mere sum over subsequent values $\mathcal{A}(\tilde{\boldsymbol{x}}_i)$:

$$\langle \mathcal{A} \rangle_\rho = \lim_{N\to\infty} \frac{|\Gamma|}{N} \sum_i^N \mathcal{A}(\tilde{\boldsymbol{x}}_i) \quad . \tag{IV.5}$$

The problem with eq. (IV.5) is that in order to pick sample points distributed as $\rho(\tilde{\boldsymbol{x}})$, the normalizing factor $\mathcal{Z} = \int_\Gamma \rho(\boldsymbol{x})\ \mathrm{d}\boldsymbol{x}$ (which equals the partition sum $\mathcal{Z}$) must be known. However, this is usually as hard as solving eq. (IV.1) itself. One solution to the problem was found by Metropolis *et al.* in 1949 [MU49]: It is possible to set up a *Markov chain* with the limiting distribution ρ.

IV.1.1 Markov Chains

A Markov chain is a mapping of a state space into itself: $\Gamma \to \Gamma\ ,\ \boldsymbol{p}^{(i)} \mapsto \boldsymbol{p}^{(i+1)}\ , i \in \mathbb{Z}$, where $\boldsymbol{p}^{(i+1)}$ just depends on the preceding value $\boldsymbol{p}^{(i)}$ (independent of the index i itself). In the case of a Monte Carlo (MC) simulation on a computer, the state space is discrete and finite [1] and we can

[1] The phase space can be thought of as divided into tiny cells whose width is e.g. given by the digital number resolution on the computer, that is, the relative uncertainty of a floating point value ϵ_M (e.g. $\epsilon_M \approx 2.2 \times 10^{-16}$ in

write the mapping as a linear function, $\boldsymbol{p}^{(i+1)} = \boldsymbol{p}^{(i)}\,\boldsymbol{\pi}$ [AT87], where the $\boldsymbol{p}^{(i)}$ are PDFs on Γ $\big($which implies $\sum_m \boldsymbol{p}^{(i)}(\boldsymbol{x}_m) = 1\big)$ and $\boldsymbol{\pi}$ is a so-called *stochastic* matrix. A quadratic matrix $\boldsymbol{\pi}$ is called stochastic, if it contains only non-negative elements and its rows add to unity [Bor76]:

$$\pi_{mn} \;\geq\; 0 \tag{IV.6a}$$

$$\sum_n \pi_{mn} \;=\; 1 \qquad \left(\Longrightarrow\; \sum_n \left(\boldsymbol{\pi}^k\right)_{mn} = 1\,, \quad k \in \mathbb{N}\right) \quad . \tag{IV.6b}$$

A Markov chain is called *irreducible* or *ergodic*, if every state vector can be reached from any other. A sufficient condition for this that the matrix be *regular*: $\pi_{mn} > 0$ [Rei80]. For ergodic stochastic matrices, the Perron-Frobenius theorem [AT87] holds which states that the largest eigenvalue of $\boldsymbol{\pi}$ is unity. The corresponding eigenvector is in our case the limiting PDF $\lim_{i\to\infty} \boldsymbol{p}^{(i)} = \boldsymbol{\rho}$

$$\boldsymbol{\rho}\,\boldsymbol{\pi} = \boldsymbol{\rho} \quad . \tag{IV.7}$$

IV.1.2 The Metropolis Algorithm

One method to solve eq. (IV.7) is to impose *microscopic reversibility*:

$$\boldsymbol{\rho}_m\,\pi_{mn} = \boldsymbol{\rho}_n\,\pi_{nm} \quad , \tag{IV.8}$$

where $\boldsymbol{\rho}_m \equiv \boldsymbol{\rho}(\boldsymbol{x}_m)$ stands for the probability to find the system in the "cell" $\boldsymbol{x}_m$ in phase space. The Metropolis algorithm sets

$$\pi_{mn} = \begin{cases} \alpha_{mn} \cdot \min(\boldsymbol{\rho}_n/\boldsymbol{\rho}_m,\, 1) & \text{if} \quad m \neq n\,, \\ 1 - \sum_{n\neq m} \pi_{mn} & \text{else} \end{cases} \tag{IV.9}$$

where $\boldsymbol{\alpha}$ is a symmetrical matrix which must not depend on the energy. The probability ratio in the canonical ensemble simulation is $\boldsymbol{\rho}_n/\boldsymbol{\rho}_m = \exp\left(-\beta\left(\Phi_n - \Phi_m\right)\right)$. Hence, the Metropolis algorithm always accepts a step which reduces/maintains the previous energy and sometimes also accepts steps which increase the energy, with a probability depending on the Boltzmann ratio. In the $T \to 0$ limit, this is therefore just equivalent to a simple minimizing algorithm, whereas for very large temperatures $k_{\mathrm{B}}T \gg \Phi$, it equals the random walk.

Since the 1940s, many refineries and variations (e.g. biased MC, isothermal MC, grand canonical MC) as well as other algorithms to satisfy eq. (IV.7), have been developed. The strength of MC lies in its simplicity and, in opposition to molecular dynamics (MD), in the total neglection of the dynamics of a system. Therefore, the MC-step index is by no means a physical timescale and consequently quantities such as velocities or acceleration cannot be computed from subsequent particle positions during the simulation. In MC, "leaps" between remote

8-bytes representation). The total number of cells is thus of the order of $(1/\epsilon_M)^d \gg d$

areas of phase space are allowed (and very favorable [AT87] – this corresponds to nonzero elements in $\boldsymbol{\alpha}$ far off the principal diagonal), since they help to ensure ergodicity. In fact, simulation efficiency decreases with mutual dependence of subsequent states, as measured by the *autocorrelation "time"* τ_A, which is assumed to be connected to the *autocorrelation function* $A(k)$ as

$$A(k) := \frac{\langle W_i \cdot W_{i+k}\rangle - \langle W_i\rangle^2}{\langle W_i^2\rangle - \langle W_i\rangle^2} = \frac{\langle W_i \cdot W_{i+k}\rangle - \langle W_i\rangle^2}{\sigma^2} \tag{IV.10}$$

$$\frac{1}{\tau_A} := \int_0^\infty A(k)\ \mathrm{d}k \qquad \Big(\text{assumption}: \quad A(k) = \exp(-k/\tau_A)\Big) \tag{IV.11}$$

where the W_i are an arbitrary data sequence with mean $\langle W_i\rangle$ and variance σ^2. A random sequence of numbers would be uncorrelated for $k > 1$ ($\langle W_i \cdot W_{i+k}\rangle = \langle W_i\rangle^2 \Rightarrow \tau_A = 1$), while $W_i = \mathrm{const}$ results in $\tau_A \to \infty$. To achieve the statistical relevance of n random numbers ("rolling dice" n times), $n_{\mathrm{ges}} = n \cdot \tau_A$ MC-steps have to be performed. Since typical subsequent MC-conformations differ very little due to system constraints, autocorrelation times of 10^4 – 10^5 steps are common and thus often of the order of 10^7 – 10^8 MC-steps are required in total.

IV.2 Discretization of Random Surfaces

The exact partition sum of a fluctuating surface with the Helfrich-Hamiltonian $\mathcal{H}[\cdot]$ is

$$\mathcal{Z} = \int \exp\big(-\beta\ \mathcal{H}[\phi]\big)\ \ \mathcal{D}[\phi] \tag{IV.12}$$

where the functional integral runs over all regular, closed, non-self-intersecting 2D-surfaces ϕ embedded in $\mathbb{R}^3$ with $A = A_0$. When solving eq. (IV.12) analytically, special attention needs to be taken to find a suitable functional gauge [CL96] in the integration to avoid counting surfaces twice.

There are numerous examples of MC simulations on random surfaces in the literature [KN87a, KN87b, BH90, HB90, BR92, Bau93, DFIJ94, IJ95, GK96, GK98]. Usually, the surface is approximated by a triangulation $\mathcal{T}_N = (\{\mathbf{X}_i\}_{i=1..N}, \mathsf{S})$, where the $\{\mathbf{X}_i\} \in \mathbb{R}^3$ are the coordinates of N vertices on the surface and S is the $N \times N$ connectivity matrix with $\mathsf{S}_{ij} = 1$ if vertices $\mathbf{X}_i$ and $\mathbf{X}_j$ are connected by a "tether" or "bond", and 0 otherwise. The bond lengths r_j are controlled by an infinite square potential

$$\begin{aligned} U_{\mathrm{bond}} &= \begin{cases} 0 & \text{if } r_{i,j} \in [r_{\min},\, r_{\max}], \\ \infty & \text{else} \end{cases} \\ r_{i,j} &:= \|\mathbf{X}_i - \mathbf{X}_j\| \quad . \end{aligned} \tag{IV.13}$$

The partition sum can now be approximated by splitting it up into an integration over the conti-

nous vertex positions in $\mathbb{R}^3$ and a sum over all possible connectivity matrices

$$\begin{aligned} \mathcal{Z}_{\mathcal{T}_N} &= \int \exp\bigl(-\beta(H[\mathcal{T}_N] + U_{\text{bond}})\bigr)\ \mathrm{d}\mathcal{T}_N \\ &= \sum_{\mathsf{S}} \int \exp\bigl(-\beta(H[\mathcal{T}_N] + U_{\text{bond}})\bigr)\ \prod_{i=1}^{N} \mathrm{d}\mathbf{X}_i \quad , \end{aligned} \tag{IV.14}$$

which is exploited by the simulation algorithm, as will be described in the next chapter.

IV.2.1 Triangulations

A body which is bound by polygons is called *polyeder*. Alternatively, one might think of a polyeder as a network of *vertices* at the polyeder corners, connected by *bonds* or *tethers* along the edges. The enclosed polygons form an orientable, piecewise smooth surface. The numbers of vertices (N), bonds (N_B), and polygons (or facets) (N_F) are connected by the Euler relation [Car83]

$$\boxed{\chi = N - N_B + N_F} \qquad \chi := 2(1-\mathfrak{g}) \qquad , \tag{IV.15}$$

where χ is called the *Euler-Poincaré characteristics* of the surface and $\mathfrak{g}$ is the surface genus (see eq. (II.3) and appendix A.2). Examples: "sphere": $\mathfrak{g}=0,\ \chi=2$, "torus": $\mathfrak{g}=1,\ \chi=0$ etc. Eq. (IV.15) is a very general relationship and holds for any kind of polyeder, even multiply connected ones. It can also be applied to flat figures if the structure is thought of as a polyeder of depth zero, in which all vertices and bonds which are not part of the outer border and all the facets are counted twice (front- and backside).

Some 3-D examples: ($\chi = 2$)

polyeder name	N	N_B	N_F
tetraeder	4	6	4
square pyramid	5	8	5
octahedron (8 triangles)	6	12	8
icosahedron (20 triangles)	12	30	20
C_{60} (soccer ball)	60	90	32
(12 pentagons, 20 hexagons)			

For closed triangulations $\mathfrak{g}=0$, where all the polygons are triangles, we thus obtain:

$$\boxed{N_F = 2(N-2)\ , \qquad N_B = 3(N-2)} \tag{IV.16}$$

(this can be interpreted in a way that except for two vertices, e.g. the two poles on the sphere, two triangles and three bonds can be assigned to each vertex).

IV.2.2 Curvature Discretization

In order to find the discretization of the Helfrich-Hamiltonian eq. (II.4) in a triangulation, consider the (smooth) surface ϕ, parametrized by $\boldsymbol{x}(u^1, u^2)$. Then for any point (u^1, u^2), a local Cartesian base (moving trihedral) can be found, as given in eq. (A.3) in the appendix. Using Weingarten's identity eq. (A.6b)

$$\partial_i \, \mathbf{n} = - \, b_i^{\ j} \, \mathbf{e}_j \quad , \tag{IV.17}$$

(where Einstein's summation convention was used), the gradient of the normal field can be expressed in local coordinates as

$$\begin{aligned} (\nabla_{\mathcal{B}} \, \mathbf{n})^2 &= (\partial_i \mathbf{n})(\partial^i \mathbf{n}) = b_i^{\ k} \, \mathbf{e}_k \, b^i_{\ l} \, \mathbf{e}^l = b_i^{\ j} \, b^i_{\ j} = \\ &= (\mathrm{Tr}\, b)^2 - 2 \det b \equiv (c_1 + c_2)^2 - 2 \, c_1 c_2 \end{aligned} \tag{IV.18}$$

(c_1 , c_2 are again the principal curvatures), and eq. (II.4) can be rewritten as

$$E = \frac{\kappa}{2} \int_\phi (c_1 + c_2)^2 \ \mathrm{d}A = \frac{\kappa}{2} \int_\phi (\nabla_{\mathcal{B}} \, \mathbf{n})^2 \ \mathrm{d}A + \kappa \underbrace{\int_\phi c_1 c_2 \ \mathrm{d}A}_{= 4\pi} \quad . \tag{IV.19}$$

Eq. (IV.19) can be approximated by a sum

$$\begin{aligned} E - 4\pi\kappa &= \frac{\kappa}{2} \int_\phi (\nabla_{\mathcal{B}} \, \mathbf{n})^2 \ \mathrm{d}A \\ &\approx \lambda\kappa \sum_{\langle \triangle_a \triangle_b \rangle}^{N_B} \left(\mathbf{n}_{\triangle_a} - \mathbf{n}_{\triangle_b} \right)^2 = \lambda\kappa \sum_{\langle \triangle_a \triangle_b \rangle}^{N_B} \left(1 - \mathbf{n}_{\triangle_a} \mathbf{n}_{\triangle_b} \right) \quad , \end{aligned} \tag{IV.20}$$

where $\langle \triangle_a \triangle_b \rangle$ denotes summation over all pairs of triangle normals between nearest-neighbor triangles $\mathbf{n}_{\triangle_a}$, $\mathbf{n}_{\triangle_b}$ (see Fig. IV.2) and the normals must have uniform orientation (e.g. pointing outside of the vesicle). There are N_B summands (one per bond) pertaining to the triangulation. A detailed comparison with a sphere, covered by uniform equilateral triangles, yields a prefactor of $\lambda = \sqrt{3}$ in the limit $N \to \infty$ [SN88, GK96]. [2] The discretization in eqns. (IV.19), (IV.20) has been used extensively in computer simulations. Recently, it was argued that λ is shape-dependent [GK96], and that a discretization based on the square of local averages of the mean curvature $H/2$ yields slightly more precise results.

[2] In the limit $N \to \infty$, $N_B/N_F = 3/2$ and $(16\pi/\sqrt{3})\,(R/a)^2$ equilateral triangles of side length a fit on the sphere of radius R. Then each pair of normals is $d = a/\sqrt{3}$ apart and the scalar products yield $\mathbf{n}_{\triangle_a} \cdot \mathbf{n}_{\triangle_b} = \cos(d/R) \approx 1 - (1/2)(d/R)^2$. Thus, the sum in eq. (IV.20) equals $4\pi\sqrt{3} \Rightarrow \lambda = \sqrt{3}$

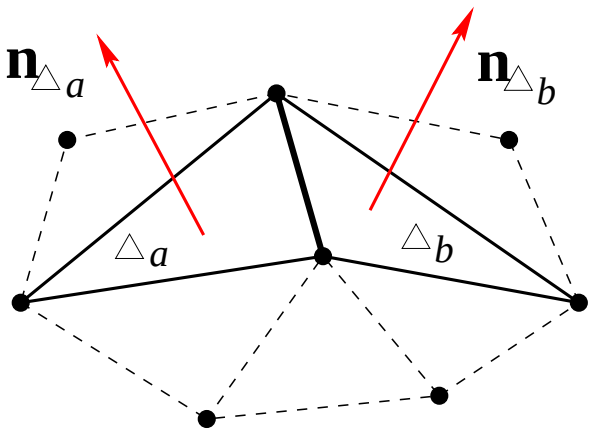

***Figure** IV.2: Two adjacent triangles $\triangle_a, \triangle_b$ on the surface ϕ with their normals $\mathbf{n}_{\triangle_a}$ and $\mathbf{n}_{\triangle_b}$.*

V. The Program

In this chapter, the MC simulation program used to simulate a fluctuating closed surface with surface inclusions will be described in detail. Next, the nature and calculation of the quantities we are interested in will be explained.

V.1 The Algorithm

The Monte Carlo algorithm used to produce the results presented in chapter VI is in part of its methods similar to various preceding examples [KN87a, KN87b, BH90, HB90, BR92, Bau93, DFIJ94, IJ95, GK96, GK98], but was completely developed from scratch in the course of this thesis. The simulation program contains about 11,000 lines of C code and runs under the UNIX operating system. For a simulation run of ca. 7.5×10^6 MCS (MCS: Monte Carlo steps) or 250 times the autocorrelation time of $\tau_A \approx 30{,}000$ MCS, around 17 CPU hours are necessary on a MIPS R10000 CPU (Silicon Graphics Indigo). The pseudo-random number generator used is the routine `ran2` in [PV88] according to L'Ecuyer with Bays-Durharn shuffle. Its period is larger than 2×10^{18}.

The MC-simulation takes place in the canonical NVT-ensemble [AT87]. It simulates a closed surface with finite bending stiffness, given by N vertices (typically $N = 500$), which are connected by $N_B = 3(N-2)$ bonds and thus enclose $N_F = 2(N-2)$ triangles (see eq. (IV.16) and Fig. V.6 at the end of this chapter). There are alternative methods of simulating a discretized 3D-surface such as going over to the const-NPT ensemble (NPT: particle number, pressure, and temperature) and taking a square, not-closed surface patch while assuming periodic boundary conditions (PBC). The linear sizes of the surface patch and thus its projected area A_p would then be the free quantity, controlled by keeping the membrane line stress σ_p and A constant, corresponding to ensemble (ii) on pg. 20. However, this implies assigning real particles to the vertices in the simulation, while in the const NVT-ensemble, no such controlling mechanism is required and thus it does not need to be specified where the microscopic lipids exactly are. Moreover, PBC are usually simulated in a box (with variable box lengths) and thus the membrane patch has to stay in this topology (and cannot, for instance, roll up into a tube etc.) In the topology of a genus-zero closed surface, none of these are problems that one has to worry about. Finally, one could think of neglecting PBC altogether and just simulate a finite membrane patch (e.g. as done in [KN87a, KN87b]). This corresponds to a cluster rather than an infinite network and can be expected to show finite-size effects. In [KN87b], this effect can indeed be seen, as a membrane

at the transition rigid/flaccid begins to crumple in the fringes first. Of course there are always finite-size effects in computer simulation. However, all parts in a closed, fluid surface are equal and thus homogeneous.

For moderate values of the bending stiffness $\kappa \geq k_{\mathrm{B}}T$, it is not necessary to explicitly employ a self-avoidance potential. Self-intersection of two remote parts of the vesicle is not impossible, but very improbable.

In order to simulate *fluid* membranes, which are thought of as 2-D fluids and therefore cannot sustain shear stress, the *bond-flip algorithm* is applied, which was first proposed and implemented by Kazakov and Kostov in 1985 [KKM85, Bil86, BH90]. A bond with its two adjacent triangles can be regarded as the diagonal in a surrounding quadrilateral (diamond). Thus, each bond can be "flipped" (rotated by about $90°$) to form two new triangles, see Figs. V.1, V.3. By virtue of eq. (IV.16), $N,\ N_B$, and N_F remain constant. If flipping is performed constantly, vertices can diffuse around the vesicle (see Fig. V.1). [1] The number of bonds that join at a vertex is constrained to lie between four and eleven (see also Fig. V.6).

In addition to the homogeneous membrane, inclusions can be simulated in it. According to the knowledge of the author, there have not been any numerical 3D off-lattice simulations of mobile inclusions on fluctuating surfaces published so far (as of August 1998). Thus, this might be the first such investigation. In the present model, rod-like inclusions are bound to a small number (typically five) vertices on the surface, thereby forcing them to align along a straight line, forming a string of vertices. Also, they are free to fluctuate along the rod, similar to water molecules next to a floating log. To ensure mutual rod-rod avoidance, rods may not intersect or share vertices. Rods are head-tail ($180°$)-symmetrical (see Fig. V.2).

One might wonder why anisotropic rods were chosen, as opposed to round or square shapes (e.g. 5×5 vertices). There are various reasons: Firstly, rod-like inclusions have a large linear length compared to their area, thus more inclusions can be simulated on the vesicle at the same time. Secondly, there are examples in biology for rod-like, directed inclusions, see chapter I. Finally, anisotropic inclusions were the subject of the Studienarbeit [Hol97] and this thesis can be regarded as a continuation thereof.

The core of the program consists of three MC-routines, representing three *move classes* or sub-sweeps:

1. Vertex moves within a cube $[-\Delta\boldsymbol{x},\ \Delta\boldsymbol{x}]^3$ centered at their former position. This corresponds to performing the integral in eq. (IV.14) (variation of $\{\mathbf{X}_i\}$).

2. Bond-flips: Variation of the connectivity matrix, thereby performing the sum over all possible S) in eq. (IV.14) (see last paragraph).

[1] In fact, every triangulation can be transformed by a sequence of bond-flips into any other with the same number of vertices N [KKM85].

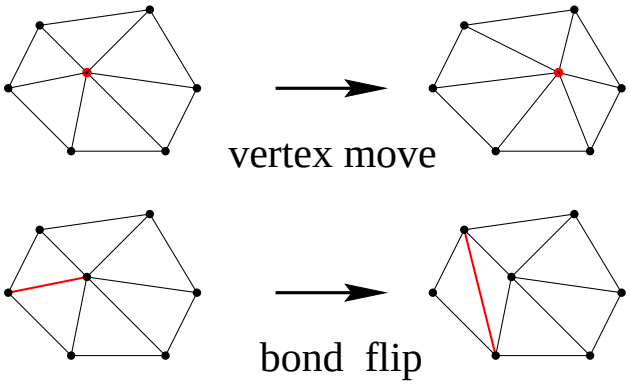

***Figure** V.1: Two different MC move classes: Vertex moves and bond-flips*

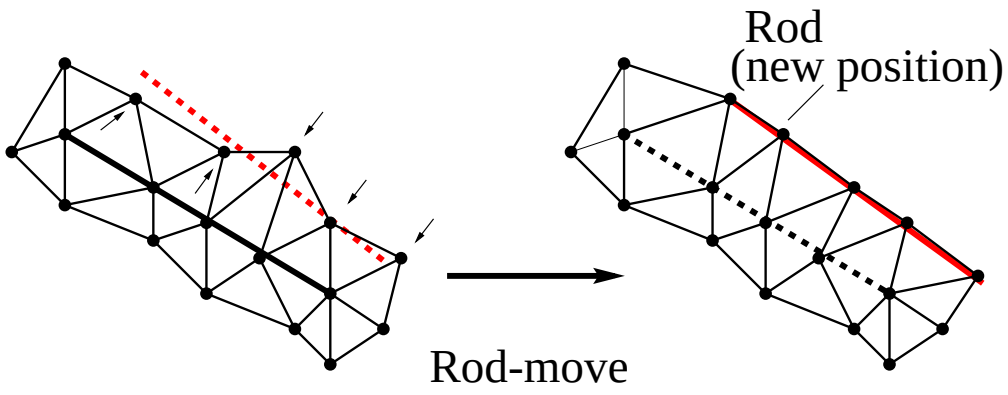

***Figure** V.2: Rod move: The rod as a whole tries to "leap" to a different set of vertices (dashed line, left picture). In the Metropolis step, the energy of the old and the new conformations are compared, where 5 new vertices have to be moved to lie on the new rod position (see arrows).*

3. Inclusion moves: Entire rods are allowed to "leap" and "land" on a nearby set of vertices.

Some kind of rod-leap is required, as the membrane is bound to static positions wherever the vertices lie on the rod. This situation is of course unphysical, since rods are not fixed in space.

It is obvious that for $\Delta\boldsymbol{x} \to 0$, every Metropolis step will be accepted (no change in conformation, constant energy). On the other hand, for very large $\Delta\boldsymbol{x}$, only few steps will be accepted, since most "proposals" lead to bond lengths outside of the square potential range. Thus, by varying $\Delta\boldsymbol{x}$, the *acceptance rate* can be adjusted. This is usually done so that around 50% of the steps are accepted. Of course this method only works for move classes with a continuous perturbation width parameter. For discrete move classes such as bond flips or rod moves for instance, acceptance rates ranged around, respectively, 10–15% and 2.5–5%.

In general, when several MC-classes are intertwined, the outcome of the simulation is independent of the order and/or relative frequency of the classes (one could, for instance, pick only $N_B/2$ bonds each time, while keeping the other sub-steps the same). However, the relaxation

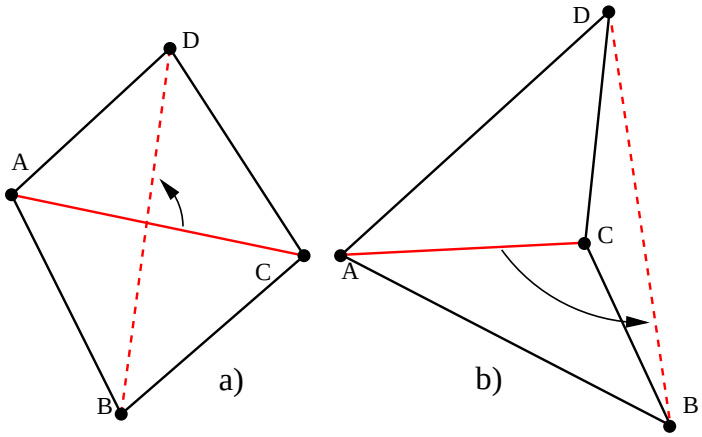

***Figure** V.3: Quadrilateral convexity in the plane: bond-flip in the convex a) and non-convex b) case. In the (forbidden) case b), the newly created triangle $\triangle_a = ABD$ includes triangle $\triangle_b = BDC$ and the triangle normals $\mathbf{n}_{\triangle_a}$, $\mathbf{n}_{\triangle_b}$ are anti-parallel. In 3D-space, the four vertices do not lie in one plane in general. In the simulation, the two new triangle normals are simply required to satisfy $\mathbf{n}_{\triangle_a} \cdot \mathbf{n}_{\triangle_b} > 0$.*

speed $1/\tau_A$ does depend on these additional choices and thus the simulation efficiency can be optimized. References concerning this problem are hard to find and test simulations can be very time-consuming. The system used in the present work is to "touch" each degree of freedom with about equal frequency: Vertex-moves are performed N times per MC-step, and N particles in 3-D space have $3N$ degrees of freedom. Out of the $N_B \approx 3N$ bonds, N bonds are randomly selected. Each bond has one degree of freedom (flip or don't), giving N degrees of freedom in total. Finally, each of the N_R rods is touched once, and a rod has two translational plus one rotational degree of freedom on the surface ($3N_R$ in total). Thus, in all three cases, we end up with ratios of $1/3$. It is important to emphasize again that e.g. vertices within one vertex-move sweep must be touched in *random order* to avoid artifacts.

There is one autocorrelation time $\tau_A[W]$ for each computed quantity W (see eq. (IV.10)). The net autocorrelation time $\tau_{A,\,\max}$ is defined as the maximum of all $\tau_A[W]$.

One might think that shear stress cannot be avoided when using a square potential which just keeps bond lengths within a certain range. This, however, is not the case since bonds in a stretched area (where the bond lengths in the stretched direction lie close to the upper bound $r_{\max}$) are more likely to be flipped and thus relax the network, than in zero-stress areas. Hence, the square potential is *on average* equivalent to a continuous (e.g. parabolic) length potential (but needs much less CPU time).

The simulations performed here do not necessarily render a physical situation in which each vertex represents one atom or lipid molecule. Rather, vertices and the connecting bonds merely state "the membrane is here", corresponding to a more general simulation in statistical mechanics. For this reason, it was possible to keep fluctuation intervals large, typically $r \in [0.5\,a,\ 1.5\,a]$ (this is larger than e.g. in [IJ95] and favorable, since $\tau_{A,\,\max} \propto (a/(r_{\max} - r_{\min}))^2$ [KN87b]). On the other hand, this implies the necessity of two additional consistency tests:

- Since $r_{\max} > 2\, r_{\min}$, triangles can "deflate", i.e. one of the vertices lies on the opposite bond (triangle has zero area). This case is avoided by requiring a minimal triangle area of e.g. $A_{\min} = (\sqrt{3}/2)\, r_{\min}^2$ (area of equilateral triangle with sides $r_{\min}$).

- When a bond is flipped, it can happen that the new, rotated bond does not lie within the surrounding quadrilateral ("diamond"). This is the case when the quadrilateral is V-shaped, or non-convex and is also forbidden (Fig. V.3).

To perform the above mentioned tasks, simulation data are stored in three separate lists, organized respectively by vertices, bonds, and triangles. The number of elements in each list remains constant, but the mutual dependence (pointer structure) is constantly changed. Each vertex has a *neighbor list* (of a length up to eleven nearest neighbors) to avoid searching for adjacent vertices and triangles.

Definition 1. ground state sphere
The ground state sphere is defined as the $\kappa \to \infty$ limit of the vesicle with its center of gravity at $\mathbf{X}_S$. Its radius of gyration will be called $R_0 := R_g(\kappa \to \infty)$. $\langle R_g \rangle$ is a little smaller than R_0 for an MC-simulation with finite κ (see eq. (III.22) *and Fig. VI.4). If the conformation of the ground state sphere is taken and its bending energy is computed for any finite value of κ, the result is that of a perfect sphere, $E_0 = 8\pi\kappa$ (see eq.* (III.17)*). The ground state sphere is the equivalent of the plane in flat topology.*

The program structure can be split up into parts:

1. **Initialization**: The triangulation $\mathcal{T}_N$ with N vertices, connected by N_B bonds (enclosing N_F triangles) are positioned on the ground state sphere. Rods are randomly distributed over the sphere, lists are initialized etc. Initialization parameters include N, N_R, $\kappa/k_{\mathrm{B}}T$, $r_{\min}$,$r_{\max}$, an estimation for the autocorrelation time $\tau_{A\mathrm{estim}}$, and how many times of this to run (n_τ).

2. **"Thermalization":** The three different move classes are iterated in a loop. One "sweep" of vertex moves (each vertex is tried to be moved once, in random order) is followed by a bond-flip sweep (N of the N_B bonds are tried to be flipped), then each rod is tried to be moved once. No quantities are computed. After ca. $10\,\tau_{A\mathrm{estim}}$, the main loop starts. The purpose of the thermalization is to lead the system with the probability $\boldsymbol{\rho}$ from the starting state (where $\boldsymbol{\rho}$ might be very small, see chapter IV) to a random point in phase space. This procedure is reminiscent of tempering a piece of cast iron (keeping its temperature close to the melting point for a while) to relax inner stresses.

3. **Main Loop**: Same as thermalization, except that after regular intervals, vesicle quantities such as curvature energy, volume, surface area, radius of gyration, correlations, magnitudes of spherical harmonics etc. (see next section) are computed and stored.

4. **Autocorrelation Test**: After $n_\tau \times \tau_{A\mathrm{estim}}$ iterations, the actual $\tau_{A,\,\max}$ is calculated from the stored data. If $\tau_{A,\,\max} > \tau_{A\mathrm{estim}}$, the missing iterations are made up to ensure a minimum statistical relevance.

5. The simulation is complete and aggregate quantities such as data variance etc. are computed.

V.2 Calculation of Physical Quantities

V.2.1 Simple Quantities

The following simple scalar properties can be computed [IJ95]:

- energy (see eq. (IV.20)):

$$E = 4\pi\kappa + \sqrt{3}\kappa \sum_{\langle \triangle_a \triangle_b \rangle}^{N_B} \Big(1 - \mathbf{n}_{\triangle_a} \mathbf{n}_{\triangle_b}\Big) \tag{V.1}$$

- surface area: sum over all triangle areas $A(\triangle_i)$

$$A = \sum_{i=1}^{N_F} A(\triangle_i) \tag{V.2}$$

- volume (the vesicle is split up into non-equilateral pyramids with the corners at 0 and the triangle corners $\mathbf{X}_{\triangle_i A,B,C}$):

$$\begin{aligned} V &= \frac{1}{3} \sum_{i=1}^{N_F} \overline{\mathbf{X}}_{\triangle_i}\, \mathbf{n}_i\, A(\triangle_i) \\ \overline{\mathbf{X}}_{\triangle_i} &:= \frac{1}{3}\Big(\mathbf{X}_{\triangle_i A} + \mathbf{X}_{\triangle_i B} + \mathbf{X}_{\triangle_i C}\Big) \end{aligned} \tag{V.3}$$

- inertia tensor:

$$\mathsf{J}^{\alpha,\beta} = \frac{1}{2N^2} \sum_{i,j=1}^{N} \Big(X_i^\alpha - X_j^\alpha\Big)\Big(X_i^\beta - X_j^\beta\Big) \tag{V.4}$$

  providing the invariants:

- radius of gyration ($\mathbf{X}_S$: center of gravity of the vesicle):

$$R_g \equiv \mathrm{Tr}\ \mathsf{J} = \left(\sum_{i=1}^{N} (\mathbf{X}_i - \mathbf{X}_S)^2\right)^{1/2} \tag{V.5}$$

- asphericity:

$$A_{\rm sp} := 1 - \frac{\min(\mathsf{J}_{(1)}, \mathsf{J}_{(2)}, \mathsf{J}_{(3)})}{\max(\mathsf{J}_{(1)}, \mathsf{J}_{(2)}, \mathsf{J}_{(3)})} \tag{V.6}$$

  ($\mathsf{J}_{(i)}$: eigenvalues of J (principal moments of inertia) , sphere: $A_{\rm sp} = 0$, disk [2] : $A_{\rm sp} = 1/2$, slim rod: $A_{\rm sp} \to 1$)

Apart from the most simple quantities such as energy, volume and surface area, the inertia tensor J provides additional structural information. Its trace equals the radius of gyration (which gives a far better effective vesicle radius than e.g. $\max(\mathbf{X}_i - \mathbf{X}_S)$). The ratio of the minimum to the maximum eigenvalue can be used to distinguish between rather spherical and more rod-like structures.

V.2.2 More Complex Quantities

- **normal–normal correlation**: In order to investigate the persistence length, the simplest approach is of course to measure $\nu(\ell)$ (eq. (III.5)) directly on the vesicle. However, one expects the ground state sphere to obey $\nu(\ell) \equiv 1$ and thus the vesicle has to be transformed into the flat state first

$$\begin{aligned} \nu_{\bigcirc}(s) \;\; &:= \;\; \left\langle \, \mathsf{D}_R\mathbf{n}(\mathbf{X}_i) \cdot \mathsf{D}_R\mathbf{n}(\mathbf{X}_j) \, \right\rangle_{\{i,j\}} \\ & \qquad s_{ij} = \|\widehat{\mathbf{X}}_i \, \widehat{\mathbf{X}}_j\|_{S^2} \quad , \end{aligned} \tag{V.7}$$

  in which $\widehat{\mathbf{X}}_i$ is the projection of vertex $\mathbf{X}_i$ on the ground state sphere (with the spherical coordinates $\{\vartheta(\mathbf{X}_i)\,,\ \phi(\mathbf{X}_i)\,,\ R_0\}$) and s_{ij} is the length of the geodesic arc between $\widehat{\mathbf{X}}_i$ and $\widehat{\mathbf{X}}_j$. Then the two normals $\mathbf{n}(\mathbf{X}_i)$, $\mathbf{n}(\mathbf{X}_j)$ are transformed into the local bases $\mathcal{B}_i$ and their scalar product is taken. All possible pairings $\mathbf{n}(\mathbf{X}_i)\,,\ \mathbf{n}(\mathbf{X}_j)$ are averaged. (Of course the shortest path between $\mathbf{X}_i$ and $\mathbf{X}_j$ in terms of the number of bonds could be determined, which would give the the exact value one is looking for. However, this procedure would be much more time-consuming. The method described above works well for $\kappa \gg k_{\rm B}T$)

- **Spherical harmonics coefficients** a_l^m can be computed by projecting the radial height field $h(\cdot)$ on the spherical harmonics (see also eq. (III.10), [Wla72]). In the case of a

[2] For a disk of radius R and mass m, the largest moment of inertia is parallel to its symmetry axis ($\mathsf{J}_{(1)} = m\,R^2/2$), while the two other, in-plane, principal moments of inertia are $\mathsf{J}_{(2),(3)} = m\,R^2/4$.

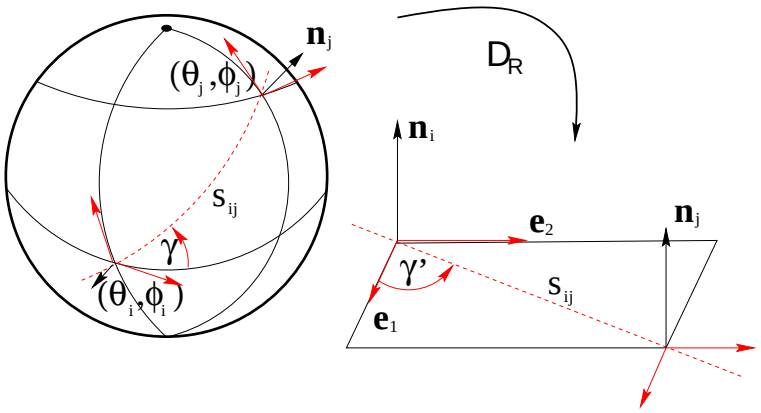

***Figure** V.4: Transformation of the triangle normals* $\mathbf{n}$ *into the local bases* $\mathcal{B}_i$ *on the ground state sphere.*

triangulation, this is written as a sum over all triangles $\triangle_i$:

$$a_l^m = \int_{S^2} h \cdot Y_l^m \, \mathrm{d}\Omega \approx \sum_i^{N_F} h_{\triangle_i} Y_l^m(\vartheta_i, \phi_i)\, \Omega_i \qquad \text{with} \tag{V.8}$$

$$h_{\triangle_i} = \frac{|\overline{\mathbf{X}}_{\triangle_i}|}{R_0} - 1\,, \qquad \Omega_i = \frac{A(\triangle_i)}{|\overline{\mathbf{X}}_{\triangle_i}|^2}\left(\frac{\overline{\mathbf{X}}_{\triangle_i}}{|\overline{\mathbf{X}}_{\triangle_i}|} \cdot \mathbf{n}_{\triangle_i}\right)\,, \quad \sum_i^{N_F} \Omega_i = 4\pi$$

$$\overline{\mathbf{X}}_{\triangle_i} := \frac{1}{3}\Big(\mathbf{X}_{\triangle_i A} + \mathbf{X}_{\triangle_i B} + \mathbf{X}_{\triangle_i C}\Big) \quad \longleftrightarrow \quad \Big\{\vartheta_i, \phi_i, R_0(1+h_{\triangle_i})\Big\}\,,$$

where the $\overline{\mathbf{X}}_{\triangle_i}$, $\mathbf{n}_{\triangle_i}$, $A(\triangle_i)$, $h_{\triangle_i}$, and Ω_i are, respectively, the triangle center, unit normal vector, surface area, normalized height field value (see eq. (III.14)), and solid angle with respect to the ground state sphere.

V.2.3 Rod-Rod Correlation Quantities

- **Mean squared rod-rod distance**: Mean squared geodesic distance $\bar{s^2}$ between rod centers on the ground state sphere (see eq. (V.7)).

- The **rod-rod pair distribution function** can be found by recording a distance-angle-histogram, i.e. the list of the number of rod-rod pairings with respect to their distance s_{12} and mutual angle $\theta := |\theta_1 - \theta_2|$. The distance is again measured similar to eq. (V.7). The probability deviation from the unperturbed case (rods diffusing on a perfect sphere with mutual avoidance) can be deduced from the pair-distribution function $g^{(2)}$ as [Hes91]

$$g^{(2)}\big(s_{12},\, \theta,\, \kappa\big) = g^{(2)}_{\mathrm{RR}}\, g^{(2)}_{\mathrm{ma}} = \exp\Big(-\beta\big(\Phi_{\mathrm{RR}}(\kappa) + \Phi_{\mathrm{ma}}(\kappa)\big)\Big)\,, \tag{V.9}$$

where $\Phi_{\mathrm{RR}}, \Phi_{\mathrm{ma}}$ are, respectively, the mutual avoidance- and interaction potentials. The angle *difference* $\theta := |\theta_1 - \theta_2|$, rather than the sum as in [GBP93, Fou96, PL96] was taken

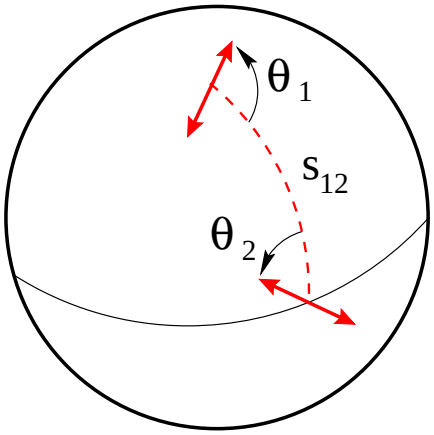

***Figure** V.5: Rod pair with (shortest) geodesic arc s_{12} on the ground state sphere.*

as the angle variable in eq. (V.9). This is because $\theta_1 + \theta_2$ is the same for perpendicular position ("T-formation") and e.g. the case $\theta_1 = \theta_2 = 45°$. However, for small distances $s < L$, the last case is essentially a side-by-side, parallel position, and thus parallel and perpendicular mutual orientations would be indistinguishable. For this reason, the angle difference is a better variable here for small s.

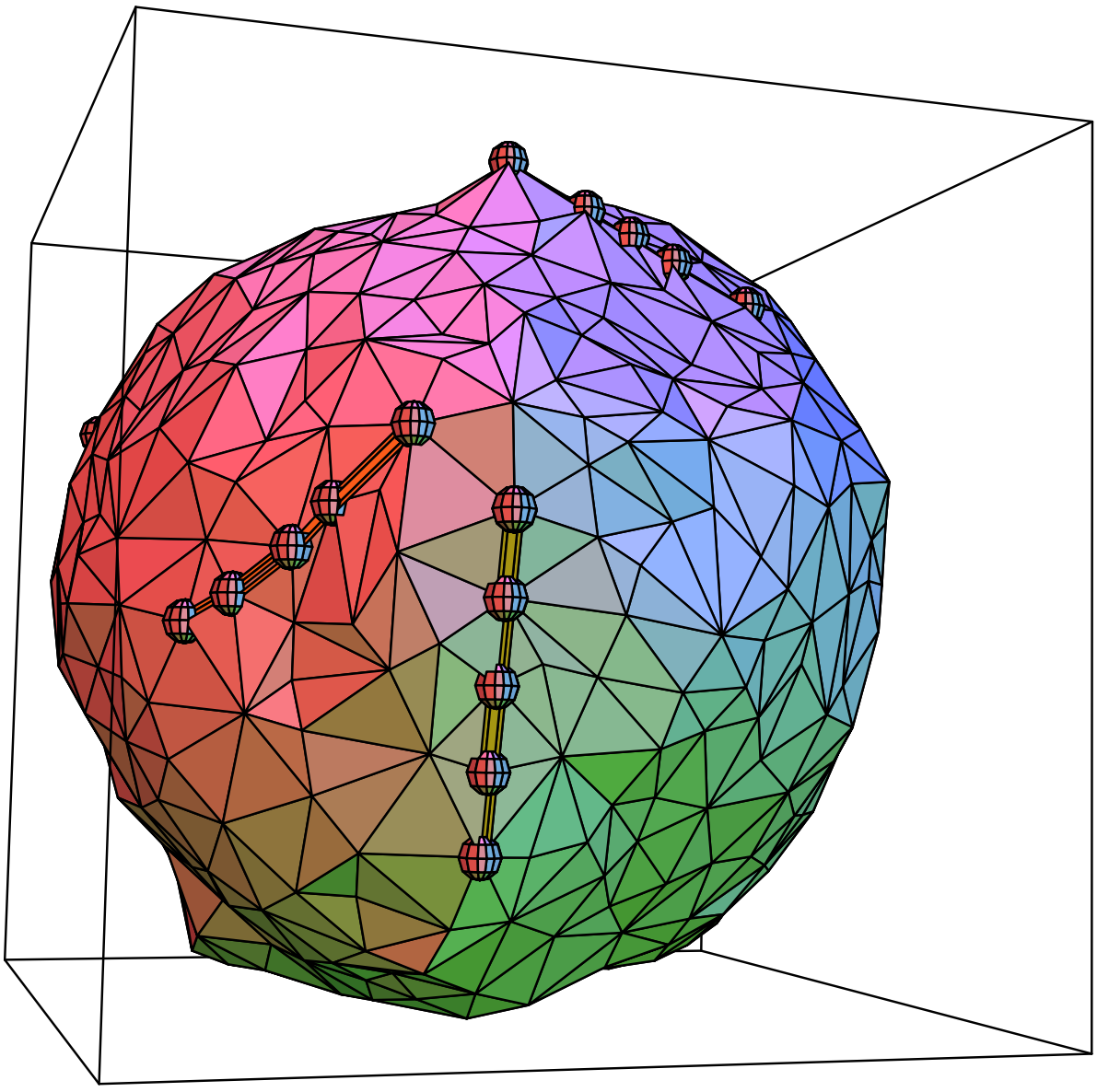

***Figure** V.6: Snapshot of a vesicle with $N = 500$ vertices, $r \in [0.5\,a, 1.5\,a]$, and $\kappa/k_{\mathrm{B}}T = 5.5$. The different colors on the surface may be thought of as reflections from three colored spotlights. The variable number of bonds that join at a vertex can be seen. Several rods are shown on the membrane, rendered by five spheres of radius $(0.5\,a)/2$ each and by tubes between them. Around the rod on the upper right side of the vesicle, one can get an impression how the membrane is locally flattened by rods.*

VI. Results

VI.1 Plain Membrane (no Rods)

VI.1.1 Simple Quantities

To verify the theoretical predictions from chapter III and for comparison with earlier found results, first a set of simulations is run on a membrane without inclusions. For all simulations, bond length limits of $[r_{\min}, r_{\max}] = [0.5\,a,\ 1.5\,a]$ are used. In the first set of eleven runs, a vesicle of $N = 500$ vertices is simulated, with bending rigidities of respectively $\kappa/k_{\mathrm{B}}T = 0.8,\ 2.0,\ 4.0,\ 7.0,\ 9.0,\ 11.0,\ 12.0,\ 13.0,\ 14.0,\ 17.0$, and 20.0. After a thermalization period of $10\ \tau_{A\mathrm{estim}}$, at least $250\ \tau_{A\mathrm{estim}}$ are performed (e.g. for $\kappa = 0.8$, that is 8.6×10^6 MC-steps).

To find out about the statistical relevance and the relaxation behavior of the different quantities, the autocorrelation functions $A(k)[W]$ are computed for the five quantities W: Energy E, vesicle volume V, surface area A, radius of gyration R_g, and asphericity A_{sp} (Fig. VI.1). The interesting result is that the autocorrelations of the asphericity and the radius of gyration decay by far least rapidly. The decay of $A(k)[R_g]$, $A(k)[A_{sp}]$ for instance seems to follow well the theoretical prediction of exponential behavior, with an autocorrelation time of e.g. $\tau_{A,\,\max} = \tau_A[A_{R_g}] \approx 32100$ MCS for $\kappa/k_{\mathrm{B}}T = 0.8$. This behavior can be understood: a change in the asphericity involves an aggregate change in the vesicle shape, e.g. from a cigar-like shape to a sphere. This requires a joint motion of all the vertices. In contrast, a change in energy can happen faster, since the local bending energy depends strongly on the amount of creases on the surface, which can be created and vanish within a few steps. Consequently, the quantities energy and also the surface area each become (auto-)uncorrelated very quickly (about $2000 - 4000$ MCS in this example). The vesicle volume shows an intermediate behavior. The above also demonstrates how important the definition and computation of the asphericity is, as it shows that structural properties relax much slower than simple scalars as the bending energy. $\tau_{A,\,\max}$ becomes smaller with increasing κ. In [Hes84], the decay behavior of simple scalar (pressure, internal energy) as well as structural (pair-correlation functions, angular order parameters etc.) quantities is measured for a fluid of particles interacting via a repulsive r^{-12}-potential. The result is similar to the present one, as it shows that "simple" quantities become auto-uncorrelated a lot faster than structural ones.

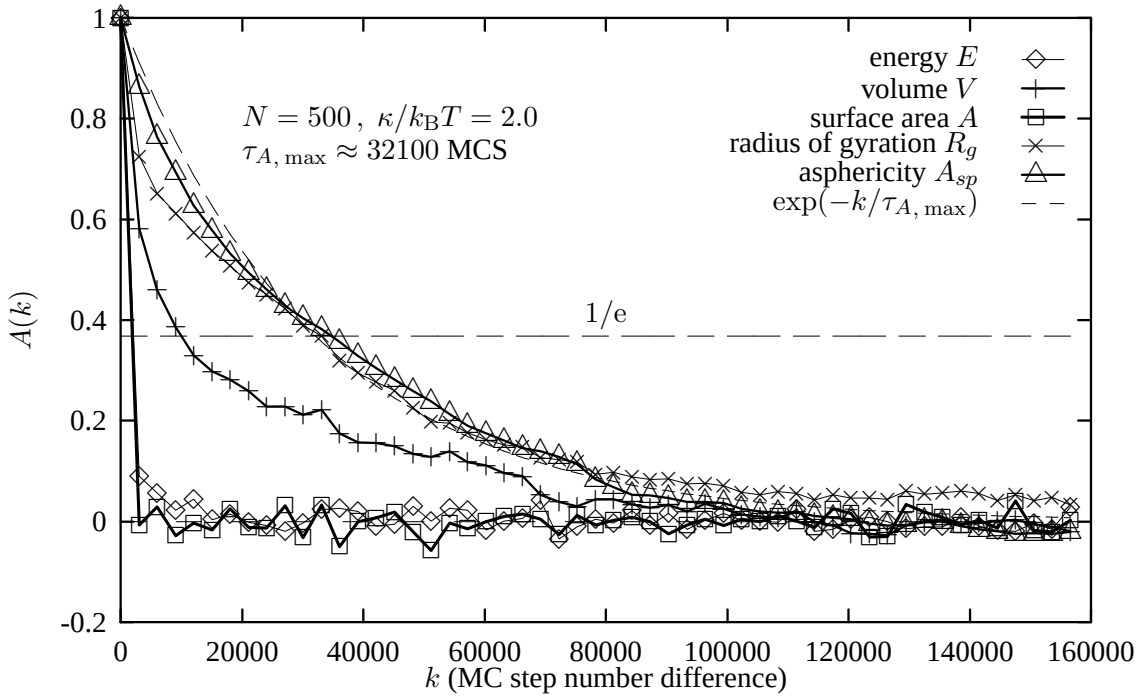

***Figure** VI.1: Autocorrelation functions for five different scalar quantities of the plain membrane. The asphericity has the largest autocorrelation time of about $\tau_{A,\,\rm max} = 32100$ MCS (see intersection of the graph with $1/{\rm e}$). The dashed curve equals the function $\exp(-k/\tau_{A,\,\rm max})$ (see eq.* (IV.11)*). The total simulation length is 8.6×10^6 MCS $= 271\ \tau_{A,\,\rm max}$. Note that the x-axis shows only the argument k of the autocorrelation function, which is a difference in MC-steps — the simulation does not "start" at $k = 0$! Rather, the autocorrelation value of e.g. $A(32100)[R_g] \approx 1/e$ means that the autocorrelation of two evaluations of R_g, being $k = 32100$ MCS apart, is $1/e$ on average.*

The uncertainty Δ of a measured quantity W is [BL85]

$$\Delta = \langle W \rangle_{\rm sim} - \langle W \rangle_{\rm exact} = \frac{\sigma[W]}{\sqrt{n_\tau}} \qquad \text{with} \quad n_\tau = \frac{n_{\rm ges}}{\tau_A[W]} \quad , \tag{VI.1}$$

where $\sigma[W]$ is the standard deviation of the quantity W and $n_{\rm ges}$ is the total number of MC steps performed.

The next plot Fig. VI.2 shows the average energies of the eleven runs. Except for the softest cases $\kappa/k_{\rm B}T = 0.8,\ 2.0$, these show a constant slope which agrees very well with the prediction of the ground state energy $8\pi\kappa + (N/2)\,k_{\rm B}T$. However, the number of degrees of freedom seems to be slightly different from the value $f = N$, see eq. (III.16) and the comment after it.

In figures VI.3 and VI.4, vesicle volume and radius of gyration are plotted against κ, expressed as fractions of the corresponding values of the ground state sphere. In order to find the values V_0, R_0, and A_0 for the ground state sphere, a simulation run is performed with $\kappa/k_{\rm B}T = 100.0$ (for larger κ, the autocorrelation times increase strongly). Both volume and radius of gyration show a very similar behavior and converge against the corresponding value

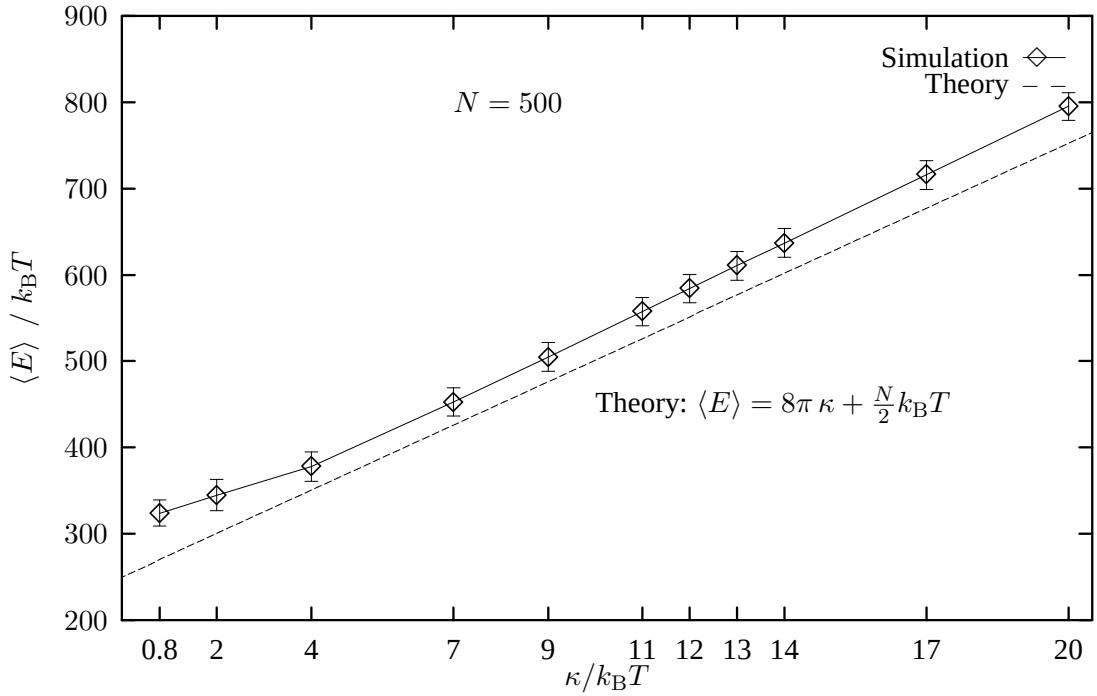

***Figure** VI.2: Comparison of eleven simulation runs with different κ with eq.* (III.18)*. The "error bars" denote the standard deviation $\sigma[E]$ of the energy fluctuations, whereas the uncertainty of the average $\langle E\rangle$ is much smaller with $\sigma[E]/\sqrt{8.6\times10^6/2000} \approx \sigma/65$. The slope of the simulation data agrees very well with the theoretical prediction (dashed curve), while the effective number of degrees of freedom seems to be slightly larger ($N/2 = f/2 \approx 280$ instead of 250).*

of the ground state sphere. The comparison with eqns. (III.21) and (III.22) shows a reasonable agreement. The gap between the theoretical prediction (dashed curve) and the measured values depends very much on the reference value that is found for the ground state sphere. Especially for quantities that show only little total variation among all different runs (e.g. 7% for R_g), the agreement is contingent on a precise determination of the ground state sphere value, as demonstrated by normalizing the data with a different value for R_0 in Fig. VI.4 (the fit for $R_0 = 5.700$ is almost perfect for larger κ — for small κ, the theory is not valid anymore). Producing more precise reference data is, however, hard to accomplish since simulations for $\kappa \to \infty$ cannot be performed. Other reasons for a deviation theory/simulation might be the relatively simple bending discretization that is used here (see last sentence in chapter IV), but also the mediocre degree of sophistication of the theory itself (eqns. (III.21),(III.22)).

Note again that the "error bars" again only show the standard deviation of the measured quantities in the simulation, not the uncertainties.

Fig. VI.5 shows the average surface areas of the eleven different runs. The true surface area (sum of all triangle areas) is hardly expected to vary very much with κ, and indeed is does only little. This would not be true for an "effective" surface area such as $4\pi {R_g}^2$.

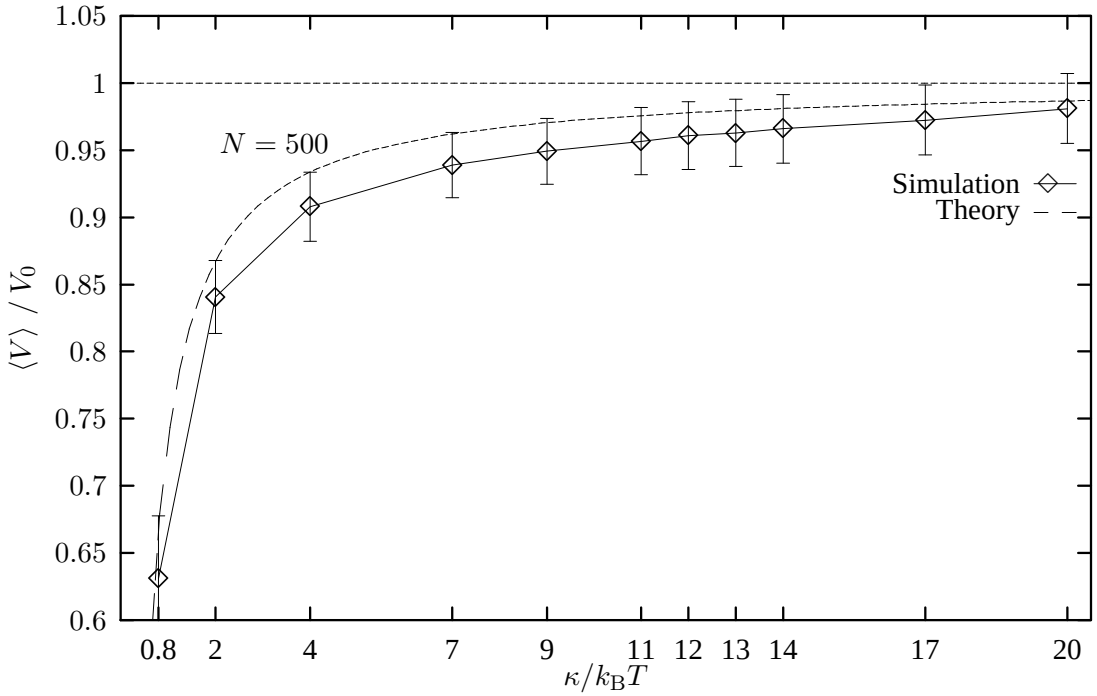

***Figure** VI.3: Vesicle volumes as fractions of the volume V_0 of the ground state sphere. With increasing bending stiffness, the vesicle volume approaches the value V_0. The "error bars" again denote the standard deviation of the fluctuations. The dashed curve shows the theoretical prediction $\langle V \rangle / V_0 = 1 - (3k_{\mathrm{B}}T)/(8\pi\kappa)\ln(l_M/2)$ with $(l_M + 1)^2 = 500$, see eq.* (III.21).

Fig. VI.6 shows the asphericities for the eleven different runs. For $\kappa < k_{\mathrm{B}}T$, extreme values can be reached. In these cases, the assumption that the vesicle fluctuates around the ground state sphere no longer holds; the membrane can, supported by the variable bond topology, form extreme buds, almost part in two bubbles (connected by a think neck) and even create deep indentations.

In Fig. VI.7, the scaling crossover of the function $\langle V \rangle \,/\, \langle A \rangle^{3/2}$ from eq. (III.9) is shown. Indeed, the slope of the breakdown is very steep around $\kappa \approx 1$. For even more flaccid membranes ($\kappa \to 0$), the self-avoidance can not be neglected any longer, since the membrane becomes so soft that it can self-intersect.

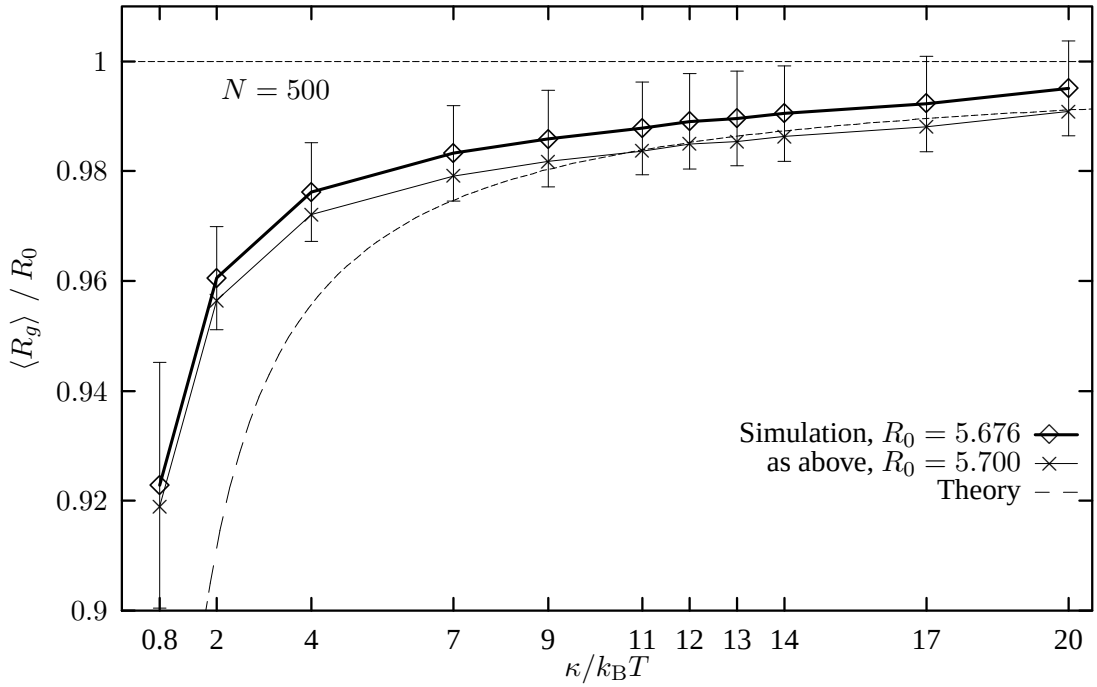

***Figure** VI.4: Radii of gyration as fractions of the radius R_0 of the ground state sphere for $R_0 = 5.676$ (from $\kappa/k_{\mathrm{B}}T = 100$) and for a slightly higher value of $R_0 = 5.740$. The behavior is very similar to that of the volume, see Fig. VI.3. The dashed curve shows the theoretical prediction $\langle R_g \rangle / R_0 = 1 - k_{\mathrm{B}}T/(4\pi\kappa) \ln(l_M/2)$ with $(l_M + 1)^2 = 500$, see eq.* (III.22).

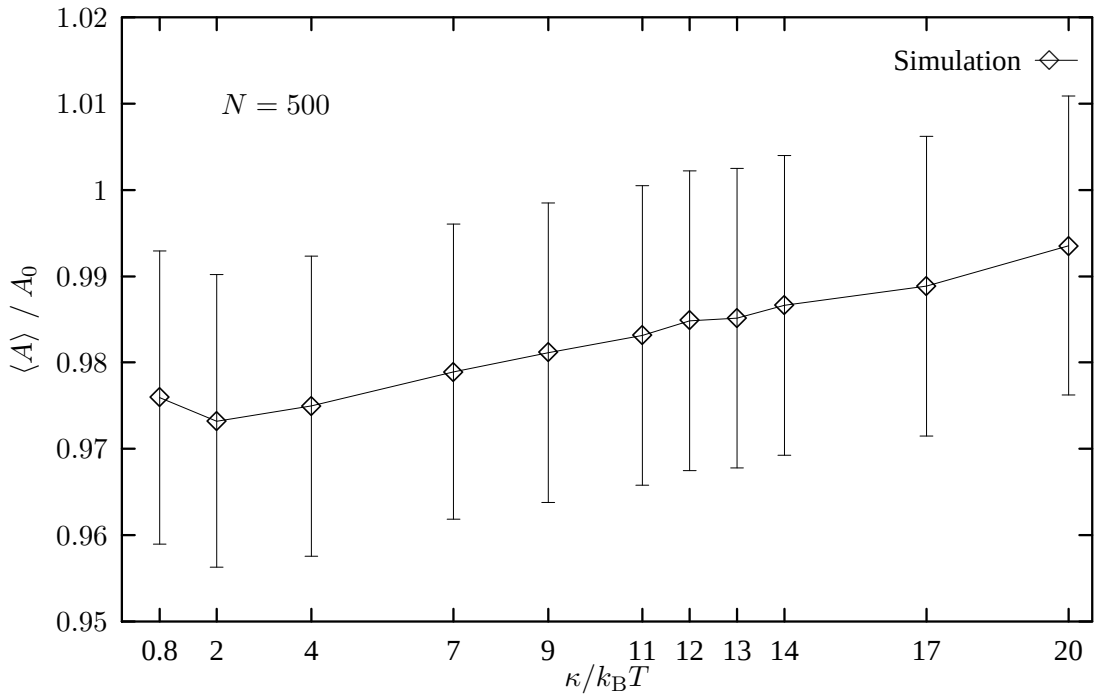

***Figure** VI.5: Vesicle surface areas as fractions of the surface area A_0 of the ground state sphere. Since A measures true surface area, it only depends weakly on κ (total variation in this plot is only about 2%). The relative standard deviation $\sigma[A]/\langle A \rangle$ is about 1.8% in all cases (see bars), showing that the simulation comes close to keeping the surface area constant.*

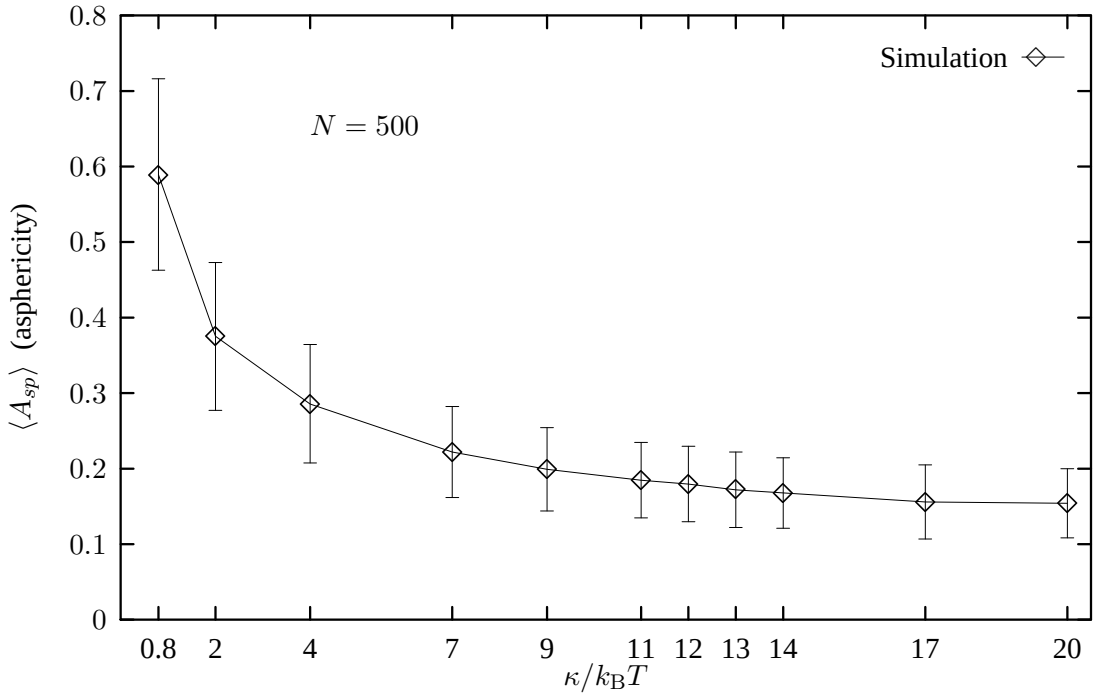

***Figure** VI.6: Vesicle asphericities. With increasing bending stiffness, the vesicle approaches the ground state sphere ($A_{sp} = 0$).*

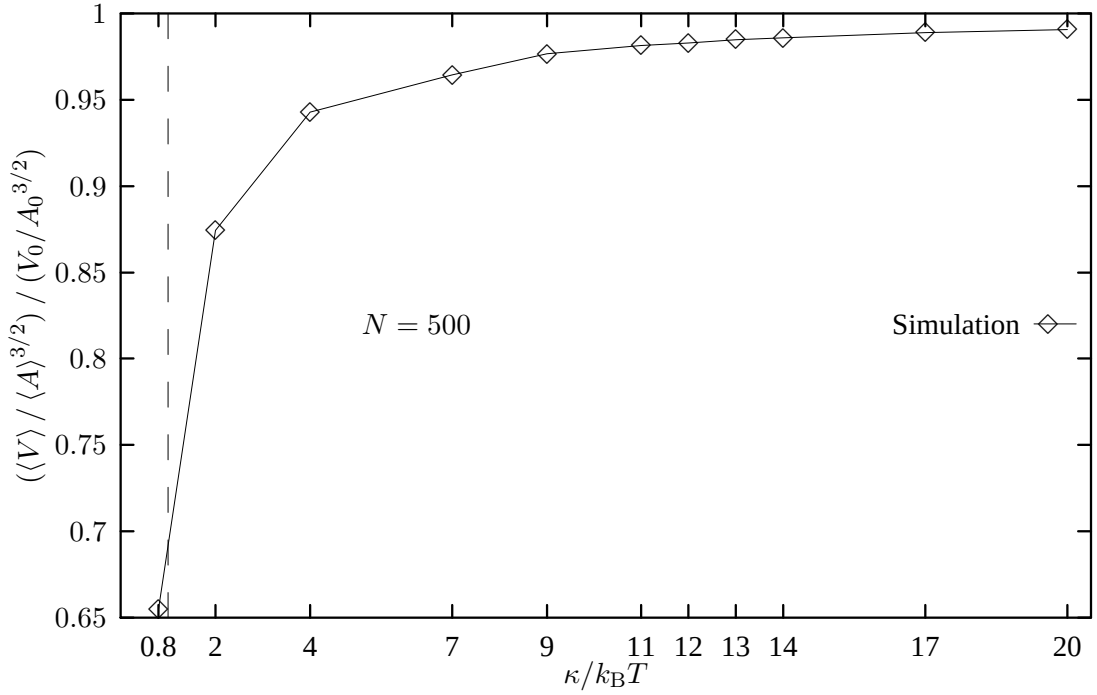

***Figure** VI.7: The function $\langle V \rangle / \langle A \rangle^{3/2}$, normalized by its value for the ground state sphere. The breakdown at $\kappa \approx 1.0$ can clearly be seen, cf. eq.* (III.9)*. This means that for $\kappa/k_{\mathrm{B}}T \approx 1.0$, the membrane persistence length ξ_M should be of the order of $\sqrt{\langle A \rangle / (4\pi)}$.*

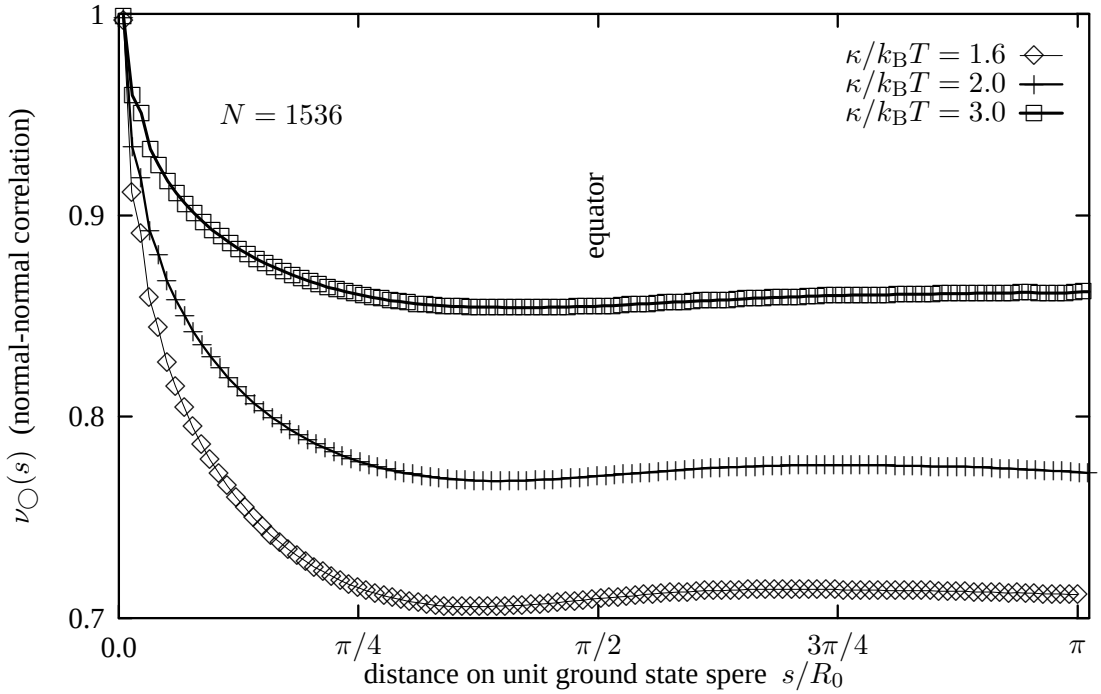

***Figure** VI.8: Normal-normal correlations of triangle normals on the vesicle $\nu_{\bigcirc}(s)$, see eq.* (V.7)*. Distances s are given as arc lengths on the unit sphere: If one of the normals in a pair is thought to lie at the north pole, a distance of $s = \pi/2$ corresponds to the other normal positioned somewhere around the equator, $s = \pi$ refers to the south pole. As discussed in chapter III, the correlation does not decay to zero, but rather converges to a finite value, increasing with κ. The slight maximums in the graphs at $s \approx 3\pi/4$ might be artifacts.*

VI.1.2 More Complex Quantities

The normal-normal correlation on the vesicle is measured directly according to eq. (V.7), the results for three different runs with $\kappa/k_{\rm B}T = 1.6, 2.0,$ and 3.0 are shown in Fig. VI.8. To achieve a higher precision, the vertex number is increased to $N = 1536$ in these simulations. The normal-normal correlation does not vanish for large separations s, but rather converges to a finite value $\nu_\infty(\kappa) = \nu_{\bigcirc}(s \to \infty, \kappa)$. This is not an artifact, but imposed by geometrical constraints, as discussed in chapter III. One can try to strip off the influence of ν_∞ by defining a normalized correlation

$$\tilde{\nu}(s) := \frac{\nu_{\bigcirc}(s) - \nu_\infty}{1 - \nu_\infty} \quad . \tag{VI.2}$$

In Fig. VI.9, $\tilde{\nu}(s)$ is plotted in the interval $s \in [0, \pi/2]$. The decay seems to be sufficiently exponential, while the slope depends very little on κ. This means that $\nu_{\bigcirc}(s)$ does only depend on κ via $\nu_\infty(\kappa)$ in this ansatz.

The last results make it hard to determine a persistence length ξ_M. In chapter III, three different definitions were given (eqns. (III.3),(III.9), (III.24)).

- The direct definition eq. (III.3) can hardly be used since $\nu_{\bigcirc}(s)$ does not follow the expo-

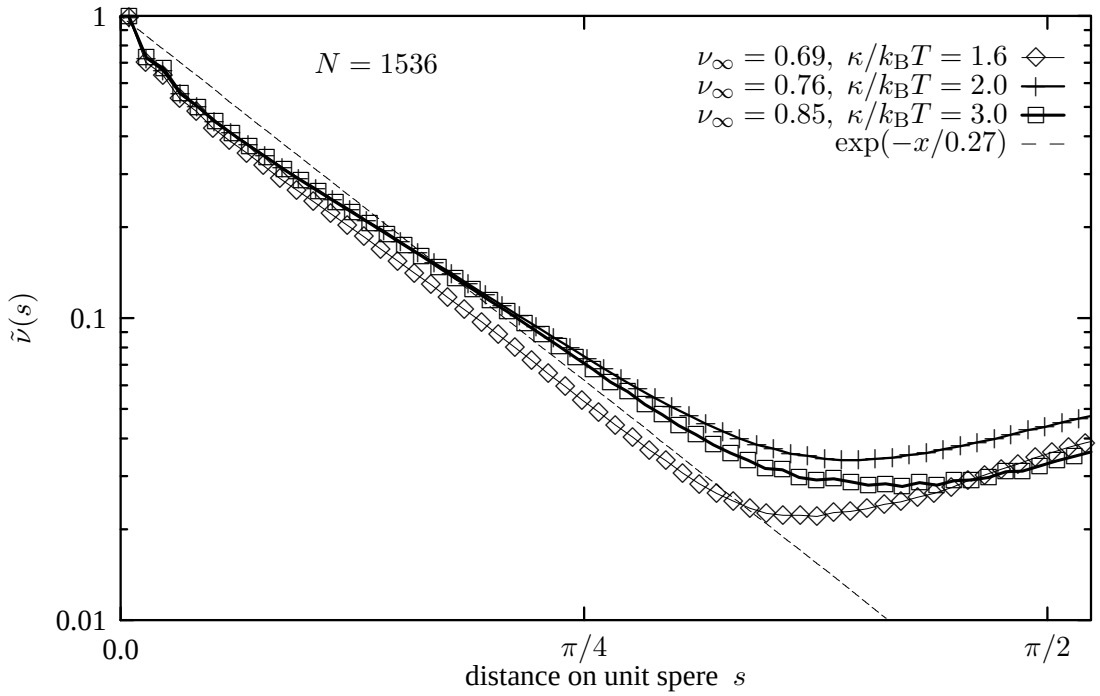

***Figure** VI.9: Semi-logarithmic plot of $\tilde{\nu}(s)$ (see eq.* (VI.2)*) in the interval* $[0,\ \pi/2]$*, plotted for the same simulations as in Fig. VI.8. The initial slope for* $s \searrow 0$ *depends very little on* κ*.*

nential law. The fact that $\nu_{\bigcirc}(s)$ never decays to zero, however, does not mean that ξ_M is infinite — the normals fluctuate around their preferred direction $\mathbf{X} - \mathbf{X}_S$ (pointing away from the center) and thus $\nu_{\bigcirc}(s)$ remains finite. However, beyond a certain distance s, they might not "feel" each other anymore, i.e., a local perturbation as from an inclusion would not have any impact.

- Eq. (III.24) crudely defines ξ_M to be of the order of the vesicle diameter when the function $\langle V\rangle \,/\, \langle A\rangle^{3/2}$ breaks down. The first series of runs with $N = 500$ is better for this test as it provides more volume data, see Fig. VI.7. The breakdown agrees with the prediction.

- Finally, according to eq. (III.24), the smallest ξ_M should be $a\ \exp(-(4\pi/3)\cdot 0.8) \approx 29\,a$ (for $\kappa = 0.8$), while for $\kappa = 2.0$, one obtains $\xi_M \approx 4300\,a$ (!).

These three reasonings do not provide an exact value for ξ_M. However, it can be deduced that the persistence length is always larger than the system size for $\kappa/k_\mathrm{B}T > 1.0$.

In figure Fig. VI.10, the result of a measurement of the magnitudes of the spherical harmonics $|a_l^m|^2$ is displayed (see eqns. (III.19),(V.8)). The vesicle with $N = 1536$ has an "equator" with a length of about $65\,a$ which is larger than the 2×12 vertices that would be at least necessary to "sample" the function $\mathrm{e}^{i\,m\phi}$ (one point per extreme, according to Nyquist's theorem, [PV88]). It

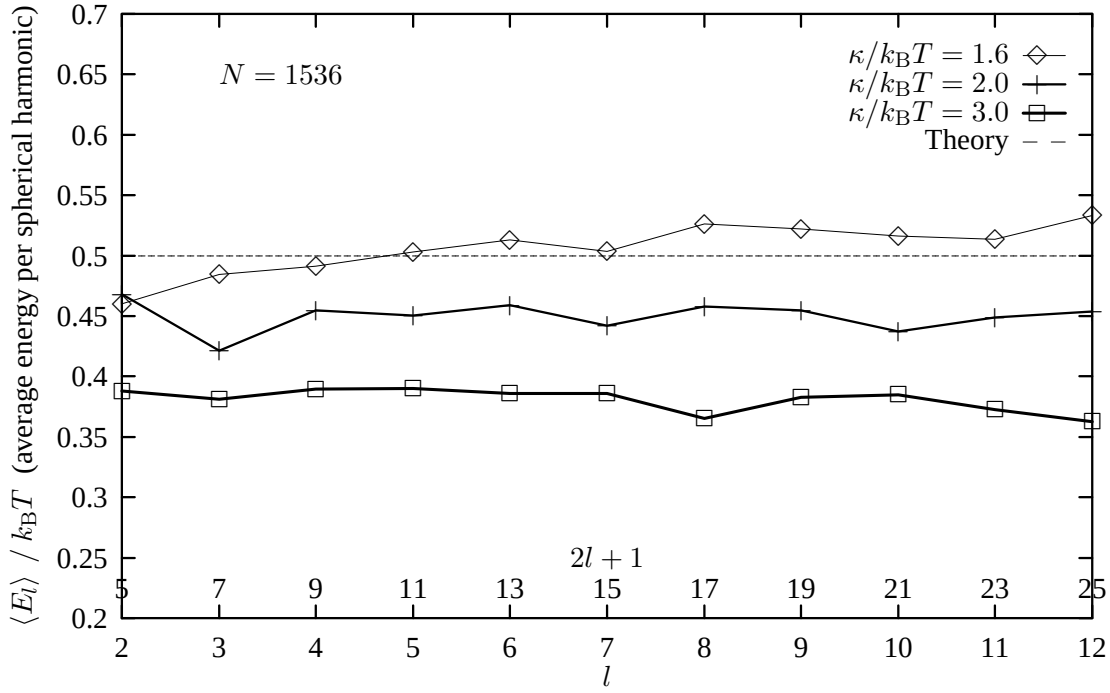

***Figure** VI.10: Magnitudes of the spherical harmonics coefficients $|a_l^m|^2$ with $2 \le l \le 12$, expressed in terms of their corresponding bending energies E_l (see eq.* (VI.3)*, eq.* (III.17)*). One data point represents the average over all $2l+1$ different values of m. The values of $2l+1$ are given above the x-axis. The agreement with theory ($E_l = k_{\rm B}T/2$) is, surprisingly, best for small κ. $(l_M+1)^2 - 4 = 165$ different spherical harmonics are used in this calculation.*

is expressed as the average bending energy in the spherical harmonics Y_l^m, $-l \le m \le l$:

$$E_l = \frac{q_l\,(q_l+2)}{2l+1}\ \frac{\kappa}{2} \sum_{m=-l}^{l} |a_l^m|^2 \quad . \tag{VI.3}$$

Given the complexity of the computation, the data agree very well with the prediction of the equipartition theorem (remember e.g. that the $|a_l^m|^2$ fall off with l as l^{-4}, see eq. (III.19)). However, it is surprising that the agreement is best for the softest membrane $\kappa/k_{\rm B}T = 1.6$ and becomes worse with increasing κ. The reason might be the small amplitudes of the different undulations on stiffer membranes which lead to larger numerical errors.

VI.2 Membranes with Inclusions

This section is devoted to MC simulations of membranes with mobile inclusions, as discussed in the last chapter. On a vesicle of $N = 500$ vertices, a set of six simulation runs is performed with $\kappa/k_{\mathrm{B}}T = 1.6,\ 2.0,\ 3.0,\ 4.0,\ 5.0,$ and 6.0 . $N_R = 6$ rods of length $L = 4\,a$ (four bond lengths) are used, which "capture" five vertices each. A brief discussion on the choice of constants will follow:

On one hand it is favorable to make the rods as long as possible to reduce discretization artifacts. On the other, long rods flatten the vesicle and locally make it deviate from the spherical shape. Also, the MC acceptance ratio goes strongly down with increasing rod size and thus relaxation speeds become a lot smaller. A length of $L = 4\,a$ seems like a reasonable compromise.

Decreasing N_R helps reducing multi-body effects (ideal for only two rods on the vesicle), however, if N_R becomes small, the quality of the statistics goes down quadratically, as there can be $N_R(N_R - 1)/2$ different pairs formed out of a set of N_R rods. With the choice $N_R = 6$ and $L = 4\,a$, 6% of the 500 vertices are covered by a rod, and L is still smaller than the radius of gyration ($\langle R_g \rangle \approx 5.5\,a$). If one assigns a disk of size $A_L = \pi(L/2)^2$ to each rod, about $N_R A_L / \langle A \rangle \approx 30\%$ of the vesicle surface are covered.

First, the autocorrelation time $\tau_A[\bar{s^2}]$ of the squared rod-rod distances $\bar{s^2}$ is calculated. Due to the "rod-leap" algorithm, $\tau_A[\bar{s^2}]$ is always lower than ca. 5000 MCS. Since this is about an order of magnitude smaller than $\tau_A[A_{sp}]$, the total simulation run lengths need not be longer than for the plain membrane.

Next, the energies of plain membranes are compared with those of membranes with inclusions (Fig. VI.11). The gap between the two curves is small, which suggests that the vesicle is not severely perturbed by the rods.

To find rod-rod interaction potentials, pair distribution functions $g^{(2)}(s, \theta)$, depending on rod-rod angle θ and geodesic center-center distance s, must be computed during the simulation. In this set of runs, a distance/angle histogram of 25×25 "slots" is used: If a rod-rod pair is found to have s and θ with

$$\frac{i}{25} \;\leq\; \frac{s}{s_{\max}} \;<\; \frac{i+1}{25} \tag{VI.4a}$$

$$\frac{j}{25} \;\leq\; \frac{\theta}{\pi/2} \;<\; \frac{j+1}{25} \qquad ,\quad i, j \in 0,\ 1,\ 2, \ldots, 24 \quad , \tag{VI.4b}$$

the number n_{ij} is incremented by one. (θ is mapped into the first quadrant so that $\theta = |\arcsin(\sin\theta)| \in [0,\ \pi/2]$). A cut-off length of $s_{\max} = 3L/2$ is used, which should in all cases be well below the membrane persistence length ξ_M (see last section).

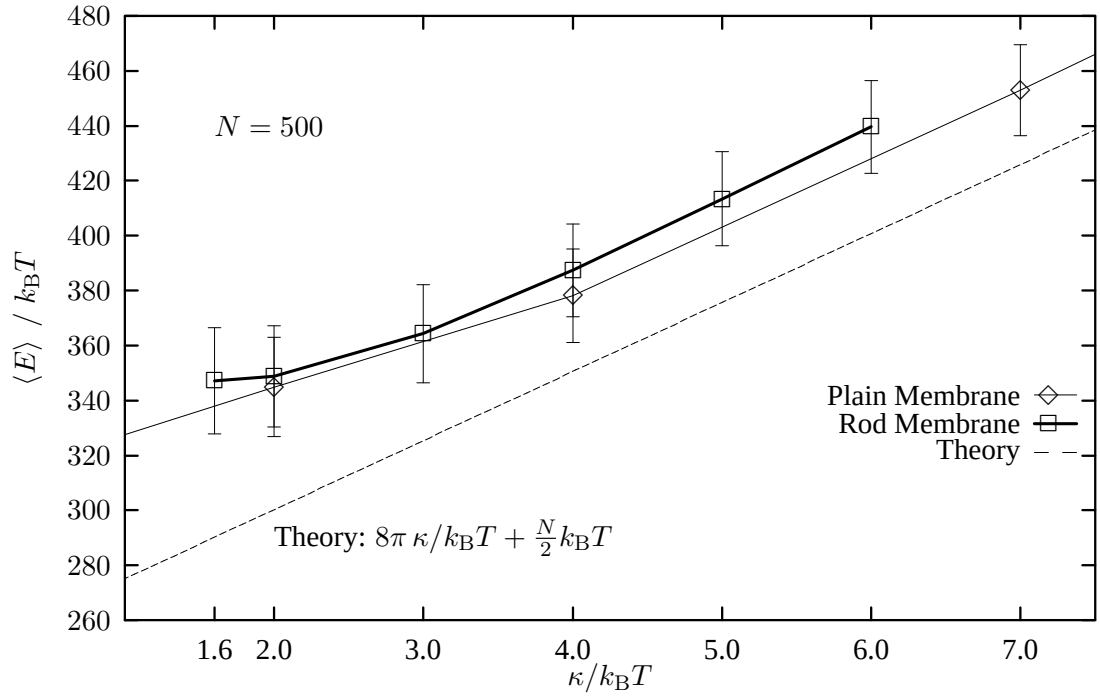

***Figure** VI.11: Comparison between energies of the plain membrane simulation and a simulation with* 6 *rods of* $L = 4\,a$ *(four bond lengths) each. The energies of the rod simulations are slightly higher than the corresponding values of the plain membrane since rods flatten the vesicle by forcing five vertices to lie on a straight line.*

The raw data n_{ij} do not become equal (independent if i, j), even after arbitrarily long simulation runs. This is because of two different reasons:

a) the accessible space (surface area) for a certain s depends on s. If rod A is thought to be at the north pole of the ground state sphere, the area of the stripe with $s - \Delta s < s < s + \Delta s$ is largest at the equator, $s = (\pi/2)\,R_0$ (see also Fig. V.5 for an illustration). In the present case, where $s_{\rm max} \ll (\pi/2)\,R_0$, the accumulated numbers n_{ij} monotonously increase with i.

b) mutual rod-rod avoidance has to be taken into account: If $s < L$, two rods can touch each other, but may not overlap (mutual avoidance), see Fig. VI.12. The part of the histogram with $\sin(\theta) > 2s/L$ is not accessible at all. The left side of the histogram refers to, both, pairs in a parallel and in-line position, while the right side ($\theta \to \pi/2$) corresponds to the "T-formation" (see Figs. VI.12 and VI.13).

The effects a) and b) can be removed from the input data in one step by normalizing n_{ij} by a reference simulation, where the rod-rod interaction due to fluctuations is somehow switched off. The method applied here is a "frozen membrane" run, where rods are simply randomly shifted around and rotated on a sphere of radius R_0. No vertices are assumed, but a move is not performed if the new rod position would overlap with another rod. A 3D-plot of the resulting

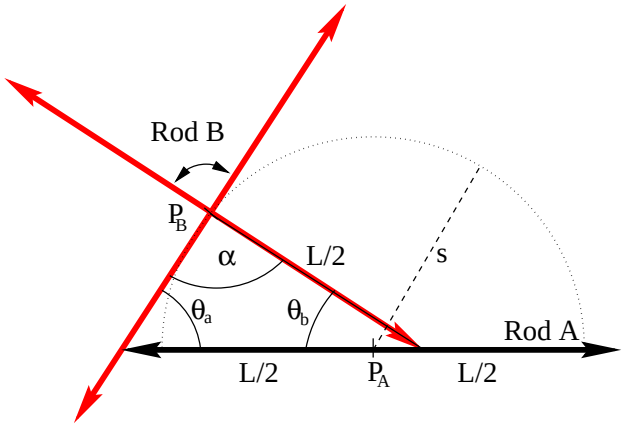

***Figure** VI.12: If two rods A and B have a center-center distance $\overline{P_A - P_B} = s$ of less than L, the usual accessible rotational angle of rod B around its center P_B of π is reduced to $\pi - \alpha = \pi - (\pi - \theta_a - \theta_b) = \theta_a + \theta_b$. For $s < L/2$, $\theta_{a,b}$ are easily computed to be $\sin(\theta_a) = 2s/L$, $\sin(\theta_b) = (4s/L)\sqrt{1/4 - (s/L)^2}$.*

histogram is shown in Fig. VI.13. In order to facilitate the assessment of the graph, the shown data result from normalizing the n_{ij} by dividing them by the corresponding stripe area on the ground state sphere. This removes effect a), see above. The forbidden area can immediately be seen in the lower right corner. Now, the rod-rod interaction potential can be calculated by

$$\frac{\Phi_{\mathrm{RR}}}{k_{\mathrm{B}}T} = -\ln\left(\frac{g^{(2)}}{g^{(2)}_{\mathrm{frozen}}}\right) \quad \Longrightarrow \quad \frac{\Phi_{\mathrm{RR}i,j}}{k_{\mathrm{B}}T} = -\ln\left(\frac{n_{i,j}}{n_{i,j,\,\mathrm{frozen}}}\right) \quad . \tag{VI.5}$$

Fig. VI.14 shows the resulting potential Φ_{RR} for $\kappa/k_{\mathrm{B}}T = 6.0$. Colored contour plots of Φ_{RR} are shown for all six runs in Figs. VI.A.1 through VI.A.6 at the end of this chapter. These results are interesting and a little amazing. First, for small distances $s \approx L/2$ and small angles (parallel side-by-side position), the most notable feature in the energy is the valley which reaches down to $\Phi_{\mathrm{RR}} \approx -2k_{\mathrm{B}}T$ for $\kappa/k_{\mathrm{B}}T = 6.0$. This indicates a strong attractive rod-rod potential; rods are more likely to align in pairs than float around by themselves. This attraction is essential in the thermodynamical sense, since it is larger in magnitude than $k_{\mathrm{B}}T$. Then, even more amazing, the T-formation is slightly repulsive for small s, with $\Phi_{\mathrm{RR}} \approx +k_{\mathrm{B}}T/4$! This means that the net membrane fluctuations can be maximized for close, parallel positions, while the T-formation seems to flatten the membrane locally and thus quench fluctuations even stronger than two separate rods would. The potential is maximally attractive for $s \approx L/4$, which equals one bond length. Rods of course cannot get closer to each other than $s = r_{\mathrm{min}}$. The attraction becomes stronger with increasing κ. However, for all of these observations, a caveat applies. Rods in the simulation do not only interact via (normal) membrane fluctuations, but also are very much influenced by lattice constraints. In this regard, it is surprising that no angular preference for $\theta = 60°$ can be found in Figs. VI.14 and VI.A.1-6 as a signature of the triangulation.

The next interesting point of course is to find out about the decay behavior: Is it exponential or does it follow a power-law? Fig. VI.15 shows $-\langle\Phi_{\mathrm{RR}}(s, \theta = 0)\rangle$ for the smallest and largest

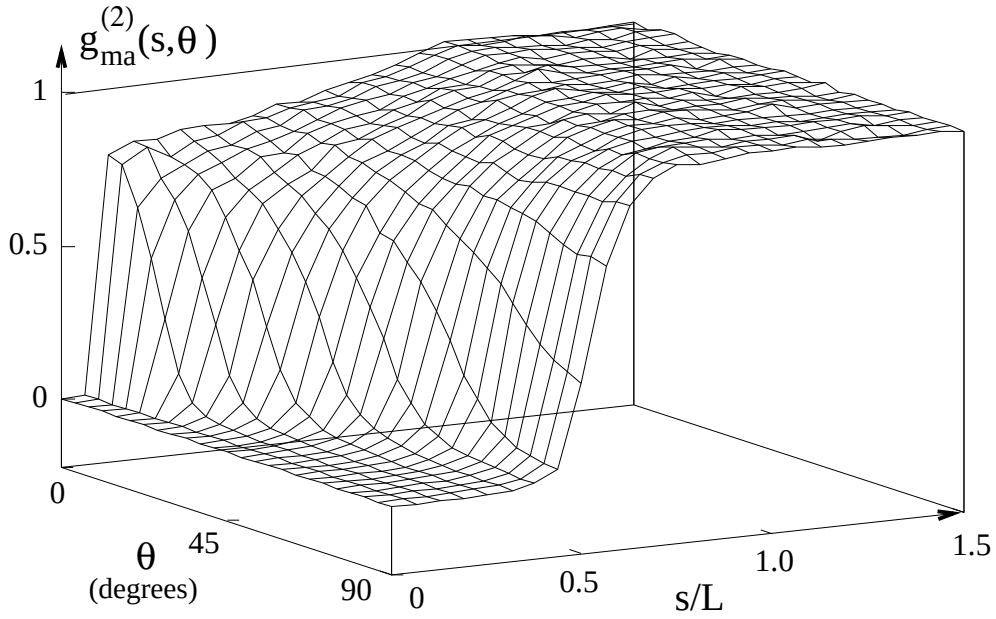

***Figure** VI.13: 3D-plot of the pair-distribution function $g^{(2)}_{\rm ma}(s,\theta)$ for the "frozen membrane" simulation. The graph is obtained by normalizing the raw histogram data n_{ij} for $L = 4\,a$ by the accessible space on the ground state sphere, depending on s (see text — without mutual avoidance, one would find $g^{(2)} \equiv 1$)*

values of κ. In both cases, the decay seems to be sufficiently exponential. Fig. VI.16 shows the dependence of κ on the depth of the minimum in $\langle\Phi_{\rm RR}(s,0)\rangle$. In the present data, this relationship is approximately linear with $\min(\langle\Phi_{\rm RR}(s,0)\rangle) \approx -k_{\rm B}T/3$.

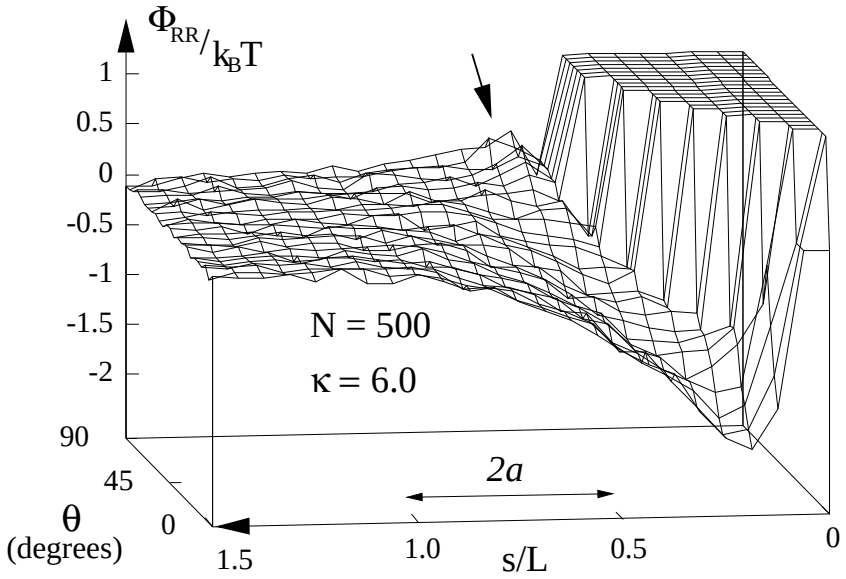

***Figure** VI.14: 3D-plot of $\Phi_{\rm RR}(s,\theta)$ for $N = 500$, $\kappa/k_{\rm B}T = 6.0$. The figure is rotated around the z-axis so that the attractive dip for $s \to 0, \theta \to 0$ lies at the right front corner. Also the repulsive hill is visible (arrow). The mutual avoidance area is the plateau in the back, $\Phi_{\rm RR}(s,\theta)$ is not defined there. The underlying histogram used to produce this plot consists of ca. $426{,}000$ data entries.*

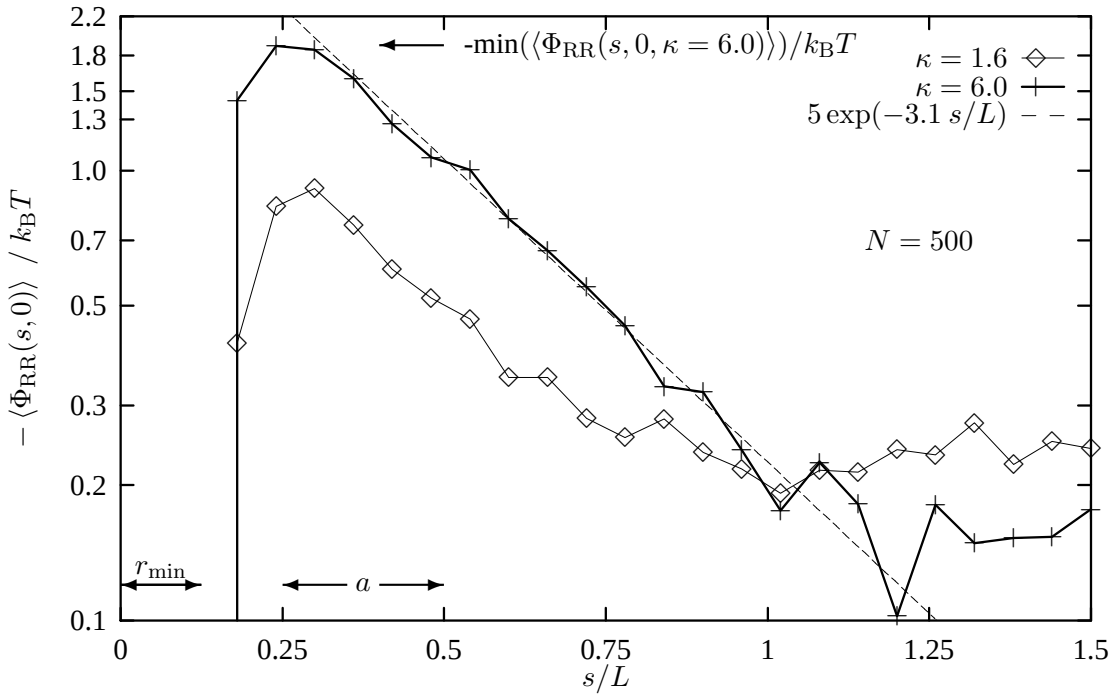

***Figure** VI.15: $-\langle\Phi_{\rm RR}(s,\theta=0)\rangle$ in semilogarithmic display, the upper curve ($\kappa/k_{\rm B}T = 6.0$) corresponds to the front row of data in Fig. VI.14. The higher the curve, the more attractive is the potential. The distance between two tics on the x-axis equals one mean bond length a ($L = 4\,a$). The exponential decay of $\Phi_{\rm RR}$ can be seen; a fit with the function $5\exp(-3.1\ s/L)$ is shown for comparison (dashed curve). For larger separations $s > L$, the curve is disturbed by noise and extremely long simulation runs would be required to obtain a smoother result. However, especially the graph for $\kappa/k_{\rm B}T = 1.6$ does not seem to converge to zero, which might indicate the presence of another, long-range force.*

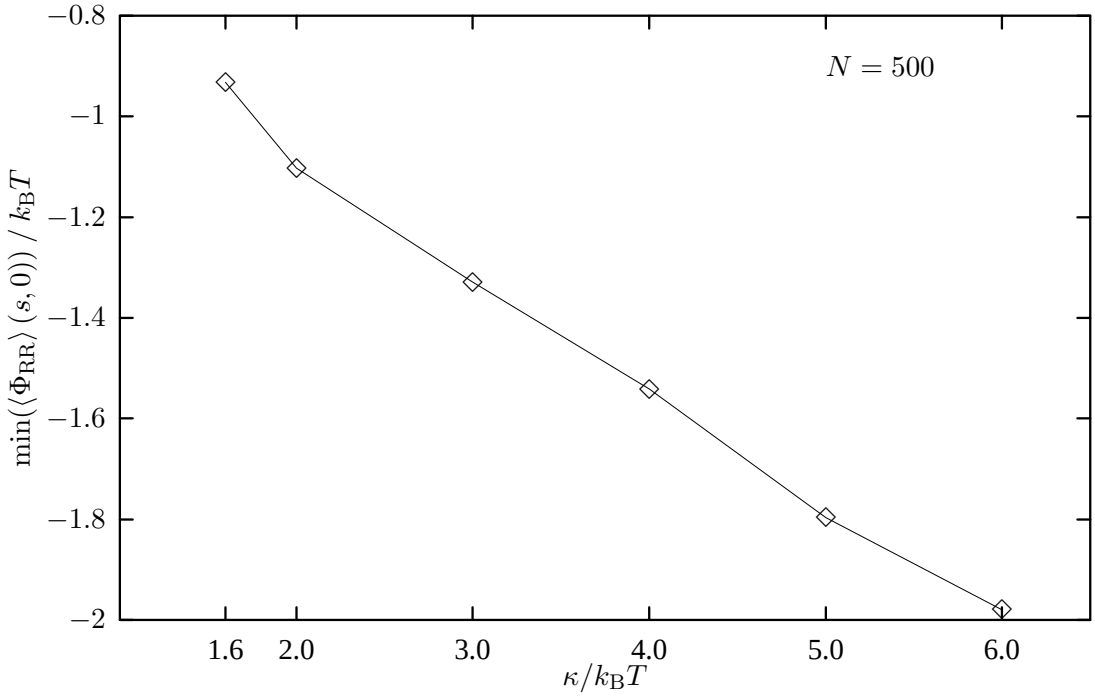

***Figure** VI.16:* $\min(\langle\Phi_{\mathrm{RR}}(s,\theta=0)\rangle)$ *vs.* κ*. The dependence is negatively linear: Inclusions on stiffer membranes feel a more attractive potential. (See also Fig. VI.15)*

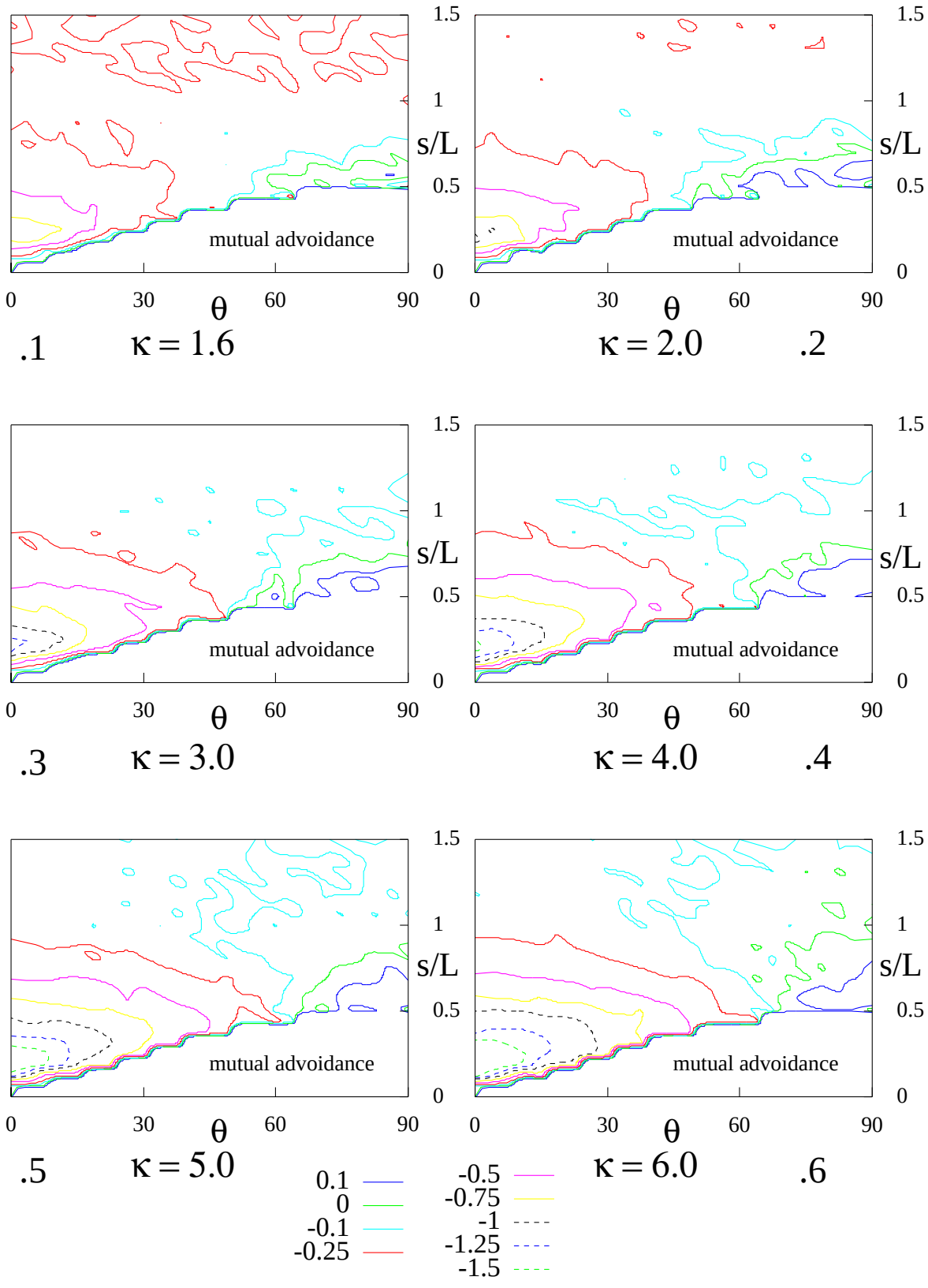

Figures VI.A.1-6 : $\Phi_{PP} / k_B T$

VII. Discussion

In the course of this thesis, a Monte Carlo program, simulating a closed, random, triangulated surface, was conceived. This surface is a simple model of a bending stiff, fluid lipid membrane. There have been numerous other related numerical simulations before, starting in the late 80s with pioneering papers [KN87a, KN87b] that reported on MC-simulations of tethered (non-fluid) membranes. The existence of a *crumpling transition* (spontaneous membrane deflation below a certain κ) and scaling behavior in general was disputed over a long time [BR89, BH90, HB90, LG90, IJ95]. Special cases such as membranes with defects [SN88], osmotic pressure [DFIJ94], fluid vesicles in shear flow [Kra96], phase diagrams for a pressure difference between vesicle in- and outside [GK94, GK95], the *freezing transition* (see chapter I) [GK97a], and, among the latest approaches, even membranes with variable surface topology [GK98] have been investigated.

However, in some regards, the present simulation is different from its predecessors:

- The algorithm with the parameter combination used is relatively fast. This might partly be due to the large bond length limits (see chapter VI), which cannot model microscopic hard spheres. On the other hand, it renders it possible to explore vesicles of up to $N = 1500$ vertices on a fast CPU.

- Due to large N, the spatial fluctuation spectrum could be computed. While there have been numerous theoretical predictions, this was perhaps never done before. The results show a good, partially very good, agreement with a quadratic approximation (see Fig. VI.10).

- (Anisotropic) inclusions have been simulated on the surface. In this regard, also the analytical side provided little insight before. The few publications [GGK96a, GBP93, Fou96, PL96] are very limited in the range of validity of their predictions. The rod-rod potential predicted in [GGK96a] is very weak and holds for large distances $s \gg L$ only. There have been no simulations at all of surface particles on vesicles in off-lattice, 3D-representation. In this work, an attempt was made to close this gap. For stiff, mobile, rod-like inclusions, an attractive exponential potential of the order of $k_{\mathrm{B}}T$ was found (see Figs. VI.15,VI.16,VI.14). Although this potential must succumb to the algebraic s^{-4}-potential in [GGK96a] beyond some distance, it dominates for small s and can bind particles together. This is relevant in biophysics as inclusion clustering was found experimentally [SG87], Fig. I.5.

Especially with respect to the last item, this simulation clearly suffers its limitations. The rod-rod potential results need to be verified for fewer, but longer (more vertices) particles on a

much larger vesicle. The surface quantization effect can be seen e.g. in Fig. VI.15, where two inclusions cannot get closer to each other than $r_{\min} = a/2$. Also, different methods of vertex/rod interaction should be compared in order to model inclusions in the most natural way. A more precise formula for the bending energy discretization, as given in [GK96], might ultimately be needed for verification. Longer runs are necessary to obtain better statistics (though this is true for any kind of simulation).

In conclusion, a fluctuating random surface as simulated here provides an interesting "lab" to monitor fluctuation phenomena in statistical physics. The combination of the lack of shear stress (fluidity) and bending stiffness is ubiquitous in nature (cell membranes), but very strange to human experience. In addition, its embedding as a 2D-manifold in 3D-space creates topological complications.

Bibliography

[Ack92] T. Ackermann, *Physikalische Biochemie*, Springer, Berlin 1992.

[AT87] M. P. Allen and D. J. Tildesley, *Computer simulation of liquids*, Clarendon Press, Oxford 1987.

[Bal81] R. Balian *et al.* (ed.), *Physics of defects*, North-Holland, 1981, (Les Houches Session XXXV).

[Bau93] A. Baumgärtner, *Phase transition of semiflexible lattice vesicles*, Physica A **192** (1993), 550–61.

[BH90] A. Baumgärtner and J.-S. Ho, *Crumpling of fluid vesicles*, Phys. Rev. A**41** (1990), 5747–9.

[Bil86] A. Billoire, *Scaling properties of randomly triangulated planar random surfaces*, Nucl. Phys. B **275** (1986), 617.

[BL85] R. Becker and W Ludwig, *Theorie der Wärme*, 3rd ed., Springer, Berlin 1985.

[Bor76] K. K. Borowkow, *Wahrscheinlichkeitstheorie*, Akademie-Verlag, Berlin 1976.

[BR89] D. H. Boal and M. Rao, *Anisotropic scaling of tethered self-avoiding membranes*, Phys. Rev. A**40** (1989), 3093–300.

[BR92] D. H. Boal and M. Rao, *Topology changes in fluid membranes*, Phys. Rev. A**46** (1992), 3037–44.

[BS87] I. N. Bronstein and K. A. Semendjajew, *Taschenbuch der Mathematik*, Verlag Harri Deutsch, Thun und Frankfurt/Main 1987.

[BW95] E. Burstein and C. Weisbuch (eds.), *Confined electrons and photons*, Plenum Press, New York 1995.

[Can70] P. Canham, J. Theor. Biol. **26** (1970), 61.

[Car83] M. do Carmo, *Differentialgeometrie von Kurven und Flächen*, Vieweg, Braunschweig 1983.

[Cas48] H. B. G. Casimir, Proc. K. Ned. Akad. Wet. **51** (1948), 793.

[CL96] W. Cai and T. C. Lubensky *et al.*, *Measure factors, tension and correlations of fluid membranes*, preprint, 1996.

[Dav88] F. David, *Hamiltonian treatment of the statistics of fluid incompressible membranes*, Europhys. Lett.**6** (1988), 603–8.

[DE86] M. Doi and S. F. Edwards, *The theory of polymer dynamics*, Clarendon Press, Oxford 1986.

[DFIJ94] B. Dammann, H. C. Fogedby, J. H. Ipsen, and C. Jeppesen, *Monte Carlo study of the inflation-deflation transition in a fluid membrane*, Jour. de Phys. II France**4** (1994), 1139–49.

[DL91] F. David and S. Leibler, *Vanishing tension of fluctuating membranes*, Jour. de Phys. II France**1** (1991), 959–76.

[För86] D. Förster, *On the scale dependence, due to thermal fluctuations, of the elastic properties of membranes*, Phys. Lett. **114 A** (1986), 115–20.

[Fou96] J. B. Fournier, *Nontopological saddle-splay and curvature instabilities from anisotropic inclusions*, Phys. Rev. Lett.**76** (1996), 4436–9.

[Fou97] J. B. Fournier, *Comment on M. Goulian et al.: "Long-range forces in heterogeneous fluid membranes"*, Europhys. Lett.**39** (1997), 681–2.

[GBP93] M. Goulian, R. Bruinsma, and P. Pincus, *Long-range forces in heterogeneous fluid membranes*, Europhys. Lett.**22** (1993), 145–50, Erratum: Europhys. Lett.**23** (1993), 155.

[GGK96a] R. Golestanian, M. Goulian, and M. Kardar, *Fluctuation-induced interactions between rods on membranes and interfaces*, Europhys. Lett.**33** (1996), 241–5.

[GGK96b] R. Golestanian, M. Goulian, and M. Kardar, *Fluctuation-induced interactions between rods on a membrane*, Phys. Rev. E**54** (1996), 6725–34.

[GK94] G. Gompper and D. M. Kroll, *Phase diagram of fluid vesicles*, Phys. Rev. Lett.**73** (1994), 2139–42.

[GK95] G. Gompper and D. M. Kroll, *Phase diagram and scaling behavior of fluid vesicles*, Phys. Rev. E**51** (1995), 514–25.

[GK96] G. Gompper and D. M. Kroll, *Random surface discretizations and the renormalization of the bending rigidity*, J. Phys. I France **6** (1996), 1305–20.

[GK97a] G. Gompper and D. M. Kroll, *The freezing of flexible vesicles of spherical topology*, J. Phys. I France **7** (1997), 1369–90.

[GK97b] G. Gompper and D. M. Kroll, *Network models of fluid, hexatic and polymerized membranes*, J. Phys.: Condens. Matter **9** (1997), 8795–834, (review article).

[GK98] G. Gompper and D. M. Kroll, *Membranes with fluctuating topology: Monte Carlo simulations*, (preprint), 1998.

[GL89] R. Goldstein and S. Leibler, *Structural phase transitions of interacting membranes*, Phys. Rev. A**40** (1989), 1025–34.

[Goe93] R. Goetz, *Monte-Carlo Simulation einer Überstruktur auf Lipidmembranen*, Master's thesis, FU Berlin, 1993.

[GT82] P. G. de Gennes and C. Taupin, J. Phys. Chem. **86** (1982), 2294.

[Hak70] H. Haken, *Laser theory*, Springer Verlag, Berlin 1970.

[HB90] J.-S. Ho and A. Baumgärtner, *Simulations of fluid self-avoiding membranes*, Europhys. Lett. **12** (1990), 295–300.

[Hei97] V. Heinrich *et al.*, *Large deviations of the average shapes of vesicles from equilibrium: Effects of thermal fluctuations in the presence of constraints*, Phys. Rev. E**55** (1997), 1809–19.

[Hel73] W. Helfrich, *Elastic properties of lipid bilayers*, Z. Naturforsch. **28c** (1973), 693–703.

[Hel85] W. Helfrich, *Effect of thermal undulations on the rigidity of fluid membranes and interfaces*, J. de Phys. **46** (1985), 1263–8.

[Hel86] W. Helfrich, *Size distribution of vesicles: The role of the effective rigidity of membranes*, J. de Phys. **48** (1986), 285–9.

[Hes84] S. Hess, *Decay of bcc-structure and of bond-orientational order in a fluid*, Physica **127A** (1984), 509–28.

[Hes91] S. Hess, *Statistical mechanics*, 1991, unpublished scriptum.

[Hil64] T. Hill, *Thermodynamics of small systems*, Dover Publications, New York 1964.

[HK80] S. Hess and W. Köhler, *Formeln zur Tensor-Rechnung*, Palm & Enke, Erlangen 1980.

[HLMZ77] W. Hoppe, W. Lohmann, H. Markl, and H. Ziegler, *Biophysik*, Springer, Berlin 1977.

[Hol97] R. Holzlöhner, *Elastomechanics of lipid membranes with anisotropic inclusions*, Inst. für Theoretische Physik, TU Berlin, 1997, Studienarbeit.

[IJ95] J. H. Ipsen and C. Jeppesen, *The persistence length in a random surface model*, J. Phys. I France **5** (1995), 1563–71.

[Isr92] J. N. Israelachvili, *Intermolecular and surface forces*, Academic Press, London 1992.

[KG97] M. Kardar and R. Golestanian, *The 'friction' of vacuum and other fluctuation-induced forces*, preprint, 1997.

[KKM85] U. A. Kazakov, I. K. Kostov, and A. A. Migdal, Phys. Lett. **157 B** (1985), 295.

[Kle86] H. Kleinert, *Thermal softening of curvature elasticity in membranes*, Phys. Lett. **114 A** (1986), 263–8.

[KN87a] Y. Kantor and D. R. Nelson, *Phase transitions in flexible polymeric surfaces*, Phys. Rev. A**36** (1987), 4020–32.

[KN87b] Y. Kantor and D.R. Nelson, *Crumpling transition in polymerized membranes*, Phys. Rev. Lett.**58** (1987), 2774–7.

[Kra96] M. Kraus, *Fluid vesicles in shear flow*, Phys. Rev. Lett.**77** (1996), 3685–8.

[Kuc91] H. Kuchling, *Taschenbuch der Physik*, Verlag Harri Deutsch, Frankfurt/Main 1991.

[LG90] R. Lipowski and M. Girardet, *Shape fluctuations of polymerized or solidlike membranes*, Phys. Rev. Lett.**65** (1990), 2893–6.

[Lip98] R. Lipowski, *Vesicles and biomembranes*, Encyc. Appl. Phys. **23** (1998), 199–222.

[LL59] L. D. Landau and E. M. Lifshitz, *Theory of elasticity*, vol. VII, Pergamon Press, London 1959.

[LM93] T. C. Lubensky and F. C. MacKintosh, *Theory of 'ripple' phases of lipid bilayers*, Phys. Rev. Lett.**71** (1993), 1565–68.

[Mac97] F. C. MacKintosh, *Internal structure in membranes: Ripples, hats, saddles, and egg cartons*, preprint, 1997.

[Man87] B. B. Mandelbrot, *Die fraktale Geometrie der Natur*, Birkhäuser Verlag, Basel 1987.

[Mes64] A. Messiah, *Quantum mechanics*, vol. I and II, North Holland Publ., Amsterdam 1964.

[ML91] F.C. MacKintosh and T.C. Lubensky, *Orientational order, topology, and vesicle shapes*, Phys. Rev. Lett.**67** (1991), 1169–72.

[MM94] D. C. Morse and S. T. Milner, *Fluctuations and phase behavior of fluid membrane vesicles*, Europhys. Lett.**26** (1994), 565–70.

[Mor94] D. C. Morse, *Topological instabilities and phase behavior of fluid membranes*, Phys. Rev. E**50** (1994), R2423–6.

[MS87] S. T. Milner and S. A. Safran, *Dynamical fluctuations of droplet microemulsions and vesicles*, Phys. Rev. A**36** (1987), 4371–9.

[MU49] N. Metropolis and S. Ulam, *The Monte Carlo method*, J. Am. stat. Ass. **44** (1949), 335–41.

[NPW89] D. R. Nelson, T. Piran, and S. Weinberg (eds.), *Statistical mechanics of membranes and surfaces*, World Scientific, Singapore 1989, (Jerusalem Winter School 1987/88).

[Pel86] L. Peliti, *Effective rigidity of membranes*, Physica A **140 A** (1986), 269–77.

[PL85] L. Peliti and S. Leibler, *Effects of thermal fluctuations on systems with small surface tension*, Phys. Rev. Lett.**54** (1985), 1690–3.

[PL96] J. M. Park and T. C. Lubensky, *Interaction between membrane inclusions on fluctuating membranes*, J. de Phys. I **6** (1996), 1217–35.

[PV88] W. H. Press and W. T. Vetterling *et al.*, *Numerical recipes in C*, 2nd ed., Cambridge University Press, New York 1988.

[Rei80] L. E. Reichl, *A modern course in statistical physics*, Univ. of Texas Press, Austin 1980.

[Sch97] M. Schoen, *Ultrathin fluid films confined to a chemically heterogeneous slit-shaped nanopore*, Phys. Rev. E**56** (1997), 4427–40.

[SG87] B. Sternberg and J. Gumpert *et al.*, *Electron microscopic and biophysical studies of liposome membrane structures . . .* , Bioch. et Biophys. Acta **898** (1987), 223–30.

[SHLU93] R. H. Simon, S. Y. Ho, S. C. Lange, and D. F. Uphoff, *Applications of lipid-coated microbubble ultrasonic contrast to tumor therapy. theory of cylindrical tubules and helical ribbons of chiral lipid membranes*, Ultrasound in Medicine & Biology **19** (1993), 123–5.

[SI89] Y. Y. Suzuki and T. Izuyama, *Diffusion of molecules in biomembranes*, Jour. of the Phys. Soc. of Jap. **58** (1989), 1104–19.

[SN88] H. S. Seung and D. R. Nelson, *Defects in flexible membranes with crystalline order*, Phys. Rev. A**38** (1988), 1005–18.

[Spi70] M. Spivak, *A comprehensive introduction to differential geometry*, Publish or Perish, Boston 1970.

[WKH98] T. R. Weikl, M. M. Kozlov, and W. Helfrich, *Interaction of conical membrane inclusions: Effect of lateral tension*, Phys. Rev. E**57** (1998), 6988–95.

[Wla72] W. S. Wladimirow, *Gleichungen der mathematischen Physik*, VEB Deutscher Verlag der Wissenschaften, Berlin 1972.

A. Some Differential Geometry

A.1 Curved Surfaces

Let ϕ be a surface $\phi \subset \mathbb{R}^3$ with the parameterization $\boldsymbol{x} = \boldsymbol{x}(u^1, u^2) = (x^1, x^2)(u^1, u^2)$. The functions x^1, x^2 may be continously differentiable twice. Then the *metric tensor* g can be defined by

$$g_{ij} := \partial_i \boldsymbol{x} \; \partial_j \boldsymbol{x} \qquad , \quad i, j = 1, 2 \quad , \tag{A.1}$$

[Spi70, Car83, BS87], F. David in [NPW89], where Einstein's convention of summing over identical indices is used and $\partial_i \equiv \partial / \partial u^i$ denotes a partial derivative with respect to the coordinate u^i. The metric tensor g is a symmetric $(0, 2)$-tensor; the elements of its inverse are written as g^{ij} ($g_{ij}\, g^{ij} \equiv \mathrm{I}$). The metric tensor and its inverse can be used to raise and lower indices, i.e. to find the components of a vector $\boldsymbol{v}$ in dual space $v^i = g^{ij}\, v_j$ [HK80]. Also, it gives the curvilinear length $\mathrm{d}s$ and area element $\mathrm{d}^2 s$ by

$$(\mathrm{d}s)^2 = g_{ij}\, \mathrm{d}u^i\, \mathrm{d}u^j \qquad \text{first fundamental form} \tag{A.2a}$$

$$\mathrm{d}^2 s \equiv \mathrm{d}A = \underbrace{\sqrt{\det \mathsf{g}}}_{=:\gamma}\; \mathrm{d}u^i\, \mathrm{d}u^j \qquad \text{surface area element} \tag{A.2b}$$

The metric tensor gives the *intrinsic* properties of a surface. However, two different surfaces (e.g. the plane and the cylinder) can have the same metric and thus g says little about the conformation of ϕ in the surrounding space.

At any point on the surface (u^1, u^2), a local Cartesian base (moving trihedral) can be found by

$$\begin{aligned} \mathcal{B}_\phi &= \{\mathbf{e}_1, \mathbf{e}_2, \mathbf{n}\} \;, \\ \mathbf{e}_i &:= \frac{\partial_i\, \boldsymbol{x}(u^1, u^2)}{\|\partial_i\, \boldsymbol{x}(u^1, u^2)\|} \quad (i = 1,\, 2) \;, \qquad \mathbf{n} = \frac{\mathbf{e}_1 \times \mathbf{e}_2}{\|\mathbf{e}_1 \times \mathbf{e}_2\|} \end{aligned} \tag{A.3}$$

with the surface unit normal field $\mathbf{n}(u^1, u^2)$. In general, $(\mathrm{d}u^1, \mathrm{d}u^2)$ induces a vector $\mathrm{d}\boldsymbol{x} \perp \mathbf{n}$ tangential to the surface. The differential of $\mathbf{n}$ along $\mathrm{d}\boldsymbol{x}$ is written as $\mathrm{d}\mathbf{n}(\mathrm{d}\boldsymbol{x})$ and also a tangential vector to ϕ. This can be used to define the *curvature tensor* b by

$$-\,\mathrm{d}\mathbf{n}(\mathrm{d}\boldsymbol{x}) \cdot \mathrm{d}\boldsymbol{x} = b_{ij}\, \mathrm{d}u^i\, \mathrm{d}u^j \qquad \text{second fundamental form} \tag{A.4a}$$

$$b_i{}^j = b_{ik}\, g^{kj} \qquad \text{curvature tensor} \tag{A.4b}$$

The curvature tensor b is a symmetrical $(1,1)$-tensor and depends on the coordinate system (u^1, u^2). However, its invariants trace and determinant are independent of this choice

$$\text{Tr } \mathsf{b} = b_i{}^i = g^{ij}\, b_{ij} = \qquad c_1 + c_2 \qquad =: H \tag{A.5a}$$

$$\det \mathsf{b} = \frac{1}{2}\Big(b_{ij}\, b^{ij} - b_i{}^j\, b_j{}^i\Big) = \qquad c_1\, c_2 \qquad =: K \tag{A.5b}$$

Here, c_1, c_2 are called the *principal curvatures* (eigenvalues of b), $H/2$ the *mean curvature*, and K *Gaussian curvature*. [Note: Often, H is defined to be the mean curvature itself, not twice of it as it is done here.]

- Gauß's and Weingarten's formulas [BS87, Car83] express the derivative of the moving trihedral

$$\partial_j \mathbf{e}_i = \Gamma_{ij}^k\, \mathbf{e}_k + b_{ij}\, \mathbf{n} \qquad \text{Gauß's formula} \tag{A.6a}$$

$$\partial_i\, \mathbf{n} = -\, b_i{}^j\, \mathbf{e}_j \qquad \text{Weingarten's identity} \tag{A.6b}$$

  where the $\Gamma_{ij}^k := \mathbf{e}_k\, \partial_j \mathbf{e}_i$ are the affine connections or *Christoffel's symbols*.

- The curvature tensor can also be defined using the *covariant derivatives* D_i

$$D_i\, v_j := \partial_i v_j - \Gamma_{ij}^k\, v_k \tag{A.7}$$

  [Spi70]. They share all the properties of conventional partial derivatives, except that they do not commute, $[D_i, D_j] \neq 0$. In this formalism, the identity

$$D_i\, D_j\, x^k = b_{ij}\, n^k \tag{A.8}$$

  [Kle86] holds.

A.2 The Gauß-Bonnet Theorem

The Gauß-Bonnet theorem may be the most fundamental one in the theory of curved surfaces [Car83]. It was first published by Gauß in 1928. Let $\boldsymbol{x}(s) \equiv \boldsymbol{x}(u^1(s), u^2(s))$ be a smooth curve on the surface $\phi \subset \mathbb{R}^3$, parameterized by its contour length. $\mathbf{n}$ may be the normal field to ϕ. Then the curvature of $\boldsymbol{x}(s)$ can be separated as

$$\frac{\mathrm{d}^2\boldsymbol{x}}{\mathrm{d}s^2} = c_n\, \mathbf{n} + c_g\Big(\mathbf{n} \times \frac{\mathrm{d}\boldsymbol{x}}{\mathrm{d}s}\Big)\ , \qquad \text{with} \tag{A.9}$$

$$c_n = \mathbf{n}\, \frac{\mathrm{d}^2\boldsymbol{x}}{\mathrm{d}s^2}\ , \quad c_g = \Big(\mathbf{n} \times \frac{\mathrm{d}\boldsymbol{x}}{\mathrm{d}s}\Big)\, \frac{\mathrm{d}^2\boldsymbol{x}}{\mathrm{d}s^2} \tag{A.10}$$

[BS87], where c_n is called *normal curvature* and c_g *geodesic curvature*. On a geodesic line, $c_g \equiv 0$.

Consider now a closed, smooth, oriented, but not necessarily simply connected part $S \subset \phi$. S may be bound by a piecewise smooth curve $\boldsymbol{x}(s)$, parameterized by its contour length s. Let $\boldsymbol{x}$ consist of smooth pieces $[s_{i-1},\ s_i]$, $i = 1, 2 \ldots k$, with angles θ_i at the corners. $\boldsymbol{x}(s)$ may run around S counter-clockwise. Then the (global) Gauß-Bonnet theorem holds

$$\sum_{i=1}^{k} \int_{s_{i-1}}^{s_i} c_g(s)\ \mathrm{d}s + \iint_S K\ \mathrm{d}A + \sum_{i=1}^{k} \theta_i = 2\pi\ \chi(S) \tag{A.11}$$

[Car83], where $\chi(S)$ is called the Euler-Poincaré characteristics of S. It is related to the *genus* $\mathfrak{g}$, which counts the number of "handles" or "holes" in S

$$\chi = 2(1 - \mathfrak{g}) \quad . \tag{A.12}$$

A closed surface has no holes, a torus would have $\mathfrak{g} = 1$, a pretzel $\mathfrak{g} = 2$, and Swiss Cheese $\mathfrak{g} \to \infty$.

A.3 Proof of eq. (II.6)

Let $\boldsymbol{x}(u^1, u^2)$ be the parameterization of the neutral surface at z_0 with $\|\partial_i \boldsymbol{x}\| \equiv 1$ and

$$\tilde{\boldsymbol{x}} := \boldsymbol{x} + \Delta z\ \mathbf{n} \tag{A.13}$$

a parallel surface separated by the normal distance $\Delta z := z - z_0$. The partial derivatives give

$$\partial_i \tilde{\boldsymbol{x}} = \partial_i\left(\boldsymbol{x} + \Delta z\ \mathbf{n}\right) = \mathbf{e}_i + \Delta z\ \mathbf{n}_{,i} \quad , \tag{A.14}$$

where partial derivatives are here denoted by a comma before the index: $\mathbf{n}_{,i} \equiv \partial \mathbf{n}/\partial u^i$ etc. for the sake of brevity. Since parallel surfaces have identical normal vector fields, we find for the corresponding surface area elements

$$\mathbf{e}_1 \times \mathbf{e}_2 \ = \ \|\mathbf{e}_1 \times \mathbf{e}_2\|\ \mathbf{n} = \gamma\ \mathbf{n} \tag{A.15a}$$

$$\tilde{\boldsymbol{x}}_{,1} \times \tilde{\boldsymbol{x}}_{,2} \ = \ \|\tilde{\boldsymbol{x}}_{,1} \times \tilde{\boldsymbol{x}}_{,2}\|\ \mathbf{n} = \tilde{\gamma}\ \mathbf{n} \quad . \tag{A.15b}$$

Combining eq. (A.14) with eq. (A.15b), we obtain

$$\tilde{\boldsymbol{x}}_{,1} \times \tilde{\boldsymbol{x}}_{,2} = \mathbf{e}_1 \times \mathbf{e}_2 + \Delta z\big(\mathbf{e}_1 \times \mathbf{n}_{,2} + \mathbf{n}_{,1} \times \mathbf{e}_2\big) + (\Delta z)^2\big(\mathbf{n}_{,1} \times \mathbf{n}_{,2}\big) = \tilde{\gamma}\mathbf{n} \tag{A.16}$$

Using Weingarten's identity eq. (A.6b) $\mathbf{n}_{,i} = -\ b_i^{\ j}\ \mathbf{e}_j$, we can write [Goe93]

$$\begin{aligned}
\tilde{\gamma}\ \mathbf{n} \ &= \ \gamma\ \mathbf{n} - \Delta z\Big(b_2^{\ k}(\mathbf{e}_1 \times \mathbf{e}_k) + b_1^{\ k}(\mathbf{e}_k \times \mathbf{e}_2)\Big) + (\Delta z)^2\ b_1^{\ k}\ b_2^{\ l}(\mathbf{e}_k \times \mathbf{e}_l) \\
&= \ \gamma\ \mathbf{n} - \Delta z\ \gamma(b_1^{\ 1} + b_2^{\ 2})\ \mathbf{n} + (\Delta z)^2\ \gamma(b_1^{\ 1}\ b_2^{\ 2} - b_1^{\ 2}\ b_2^{\ 1})\ \mathbf{n} \\
&= \ \gamma\Big(1 - \Delta z\ \mathrm{Tr}\ b + (\Delta z)^2\ \det b\Big)\ \mathbf{n} \\
\Rightarrow \tilde{\gamma} \ &= \ \gamma\Big(1 - \Delta z\ H + (\Delta z)^2\ K\Big) \quad .
\end{aligned} \tag{A.17}$$

Therefore, we obtain for the relative change in surface area at z

$$\delta A := \frac{A(z) - A(z_0)}{A(z_0)} = \frac{\tilde{\gamma} - \gamma}{\gamma} = -(z - z_0)\, H + (z - z_0)^2\, K \quad . \tag{A.18}$$

□

Zusammenfassung

In dieser Arbeit werden die mesoskopischen und statistischen Eigenschaften fluktuierender Membranen untersucht. Das wichtigste Verfahren dazu ist eine Monte Carlo Simulation einer geschlossenen, fluiden Oberfläche mit Biegesteifigkeit. Diese stellt ein stark vereinfachtes Modell einer Lipidmembran dar, wie man sie z.B. in den Wänden biologischer Zellen findet. Geschlossene Lipidmembranen werden auch als „Vesikel“ bezeichnet. In der Simulation wie in der Natur fluktuiert das Vesikel nun um einen kugelförmigen Grundzustand; die Abweichungen von der Kugelform werden dabei durch die Größe der Biegesteifigkeit bestimmt.

Die Membran wird durch eine dynamische Triangulierung diskretisiert, also ein Netzwerk von durch Stäben verbundenen Punkten, die jeweils Dreiecke einschließen. Zahlreiche Parameter der Membran wie Biegeenergie, Oberflächeninhalt, Korrelationen der Oberflächennormalen etc. werden berechnet. Außerdem wird die Deformation des Vesikels in Kugelflächenfunktionen entwickelt und auf diese Weise das Fluktuationsspektrum bestimmt. Für alle diese Ergebnisse gibt es theoretische Vorhersagen, mit denen sie verglichen werden. Der Vergleich ergibt in allen Fällen eine zufriendenstellende Übereinstimmung, z.T. auch eine gute und sehr gute.

In einer Erweiterung der reinen Membran werden eingebettete unbiegsame, stäbchenförmige Einschlüsse auf ihr simuliert, die die thermischen Membranfluktuationen lokal stören. Dadurch kommt es zu Wechselwirkungen zwischen den Einschlüssen, die durch die Membran vermittelt werden. Diese werden durch ein Distanz-Winkel-Histogramm gemessen, und mit Hilfe eines Normierungslaufes wird ein effektives Wechselwirkungspotential berechnet.

Die Einleitung und Kapitel I definieren den Begriff der biologischen Membranen und führen in deren physikalische Eigenschaften ein. Kapitel II leitet einen Ausdruck für die Biegeenergie der Membran her, unterstützt durch mikroskopische Betrachtungen des Membranquerschnittes. In Kapitel III werden einige thermodynamische Eigenschaften von Lipidmembranen besprochen und charakteristische Längen definiert. Kapitel IV behandelt die theoretischen Grundlagen der Monte Carlo Simulation und Kapitel V beschreibt Einzelheiten des Simulationsprogrammes. Die Ergebnisse der Simulation werden in Kapitel VI präsentiert und in Kapitel VII diskutiert und in Ihrer Bedeutung gewerted.

Ein mathematischer Anhang befasst sich in kurzer Form mit der Theorie gekrümmter Flächen.

Danksagung

Mein besonderer Dank gehört meinem Betreuer, Herrn Prof. Dr. S. Hess, und Herrn Dr. rer. nat. habil. M. Schoen, die mich immer in sehr fairer und freundlicher Weise in meiner Arbeit unterstützt haben. Darüber hinaus haben mir Dr. Martin Kröger, Dipl. Phys. Thomas Gruhn und Dr. Claus Jeppesen (UC Santa Barbara) bei vielen Detailfragen zur Simulation und der Physik geholfen. Dipl. Phys. Loris Bennett half mir bei einigen sprachlichen Zweifelsfällen. Herrn Dr. G. Gompper (Max-Planck-Institut für Kolloid- und Grenzflächenforschung, Teltow) verdanke ich fruchtbare Diskussionen zu Fragen der Diskretisierung und der Fluktuationsfreiheitsgrade eines Vesikels.

Für das Korrigieren des Manuskripts danke ich Dr. habil. Schoen, Dr. Kröger, meinem Vater Dr. U. Holzlöhner und Heather Simon.

Darüber hinaus danke ich J. B. Fournier (ESPCI Paris) und Prof. Phil Pincus (UC Santa Barbara) für die Einführung in das Themengebiet.

Am Ende gilt mein Respekt Donald E. Knuth, Leslie Lamport und allen anderen, die das Satzsystem TEX geschaffen haben, in dem diese Arbeit geschrieben ist.